Double perovskite (Sr$_2$B′B″O$_6$) oxides for high-temperature thermoelectric power generation—A review

Tanmoy Maiti,[a)]Mandvi Saxena, and Pinku Roy
Plasmonics and Perovskites Laboratory, Department of Materials Science and Engineering, Indian Institute of Technology Kanpur, Uttar Pradesh 208016, India

Recently, double perovskite-based oxide materials have been proposed for thermoelectric (TE) applications due to their environment-friendly nature, high-temperature stability, better oxidation resistance, and lower processing cost compared to conventional chalcogenides and intermetallics. In this review article, we have comprehensively summarized our recent research studies on Sr$_2$B′B″O$_6$-based double perovskites for high-temperature TE power generation. We have shown that decoupling of phonon-glass and electron-crystal behavior is possible in oxides by reducing thermal conductivity due to induced dipolar glassy state as a result of relaxor ferroelectricity. We have also introduced metal-like electrical conductivity ($\sim$10^5 S/m) in these ceramics that are inherently insulator in nature. Moreover, we have observed interesting behavior of temperature-driven p–n type conduction switching assisted colossal change in thermopower in some of these oxides, hitherto, obtained only in chalcogenides. The charge transport mechanism in these complex oxides has been analyzed by small polaron hopping conduction model in conjugation with defect chemistry.

Dr. Tanmoy Maiti is an Associate Professor in the Department of Material Science and Engineering at the Indian Institute of Technology Kanpur, India. Dr. Maiti received his Ph.D. in Materials Science and Engineering from The Pennsylvania State University, University Park, PA, USA, in December 2007. He earned his Masters Degree in Ceramic Engineering from Institute of Technology, BHU in 2004 and Bachelors in Ceramic Technology from College of Ceramic Technology, University of Calcutta in 2002. Prior to joining IIT Kanpur in 2010, he did his post-doctoral research in Lawrence Berkeley National Laboratory and Pennsylvania State University. He specializes in electronic materials and nanophotonics. Prof. Maiti has formed his research group in newly set-up Plasmonics and Perovskites Laboratory at IIT Kanpur. His research interests span the areas of Thermoelectrics, Plasmonics, Photovoltaics and Oxide electronic materials and devices. However, a common thread in his research is to address (i) the global energy problem by developing novel materials for clean energy generation (e.g., thermoelectric power generator, perovskite solar cell) and (ii) the design of next generation chip-scale technology based on nanophotonics and nano-electronics (e.g., optical memory based on plasmonic lenses and RRAM).

Tanmoy Maiti

I. INTRODUCTION

Energy is one of the most important core requirements for the progress of modern civilization. As of today, most of our energy demand is fulfilled by the supply of fossil fuels. Burning the fossil fuels for energy generation has been shown to be one of the reasons behind global warming and climate change. Interestingly, only one-third of the primary energy input is utilized efficiently, and two-third of it is wasted in the form of heat.[1,2] Hence, it is desirable to develop an energy conversion device that can produce electricity using the huge amount of waste heat generated from automotive exhausts, industrial processes, and residential heating. Thermoelectric (TE)

power generation offers a fascinating prospect as it transforms thermal energy (waste heat) into electrical energy using the Seebeck effect. Moreover, it is a solid-state device without any moving parts, offering great flexibility in operational integration.[3,4] The performance of a TE device is generally evaluated by a figure-of-merit called *ZT*, which corresponds to the intrinsic properties of the material as expressed by the following equation:

$$ZT = \frac{S^2\sigma}{\kappa}T = \frac{S^2\sigma}{\kappa_e + \kappa_l}T \quad , \qquad (1)$$

where S is the Seebeck coefficient, σ is the electric conductivity, κ is the thermal conductivity, and T is the temperature. Thermal conductivity has a contribution from two parameters namely electrical thermal conductivity (κ_e) and lattice thermal conductivity (κ_l). A good TE material with a high *ZT* value requires a high Seebeck

coefficient (*S*), high electrical conductivity (σ), and low lattice thermal conductivity (κ). The primary obstacle to increase *ZT* is that these fundamental properties of materials are interconnected. As a result, enhancing one property deteriorates the others.

Conventional TE materials are based on chalcogenides such as Bi$_2$Te$_3$,[5] Sb$_2$Te$_3$,[6] Zn$_4$Sb$_3$,[7] Bi$_2$Se$_3$,[8] and SnTe.[9] However, most of the waste heat generated from various sources is >900 K and these materials decompose and oxidize at such high temperatures. Oxides are a better alternative for high-temperature TE applications due to their low costs, and higher oxidation resistance with better thermal stability.

Recently oxide TE materials[10,11] such as Na$_x$CoO$_2$, Ca$_3$Co$_4$O$_9$, etc. showed good *ZT* values with p-type conductivity. However, their *ZT* values are not comparable with the conventional chalcogenides. Besides, there are not many options available among oxide-based materials, to choose as n-type element in the TE module. It is beneficial to have both n-type and p-type oxides with good *ZT* values to reduce the strain mismatch in the TE module in which n-type and p-type materials are connected thermally in parallel and electrically in series.[12] In recent years, Nb and La-doped SrTiO$_3$ perovskite-based n-type materials showed very promising high-temperature TE properties, but their *ZT* values need to be improved to be considered for commercialization.

In the present work, we hypothesize that SrTiO$_3$-based double perovskites (Sr$_2$TiB′O$_6$) are environmentally friendly high-temperature TE materials. Double perovskite materials were extensively investigated over the years for their wide range of exciting properties,[36–40] e.g., colossal magneto-resistance, ferroelectricity, multiferroicity, high *T$_c$* superconductivity, multi-band Mott insulators, and half-metallic behavior. A$_2$B$_2$O$_6$ double perovskites are very amenable to compositional modification, whereby using different types of B site cations, their electrical, magnetic, and thermal properties can be tailored. Furthermore, these materials have complex crystal structure capable of accommodating multiple cations, which can act as phonon scattering centers required for low lattice thermal conductivity. Although some papers reported[13–15,17,18] on TE properties of double perovskites as presented in Table I, most of these materials were primarily designed for investigating magnetoresistance, mutiferroics properties.

Recently, we published a series of papers on SrTiO$_3$-based double perovskites for high-temperature TE application. We showed that by selecting appropriate elements for A-site and B-site cations in A$_2$B$_2$O$_6$ double perovskite and manipulating the dopant concentrations along with optimized processing parameters,[24,25] one can achieve very large thermopower,[19,22,41] metal-like electrical conductivity,[24–26] and glass-like thermal conductivity.[22] In this article, we present a comprehensive review on the recent progress of Sr$_2$B′B″O$_6$-based double perovskites

for high-temperature TE applications and the future direction. We demonstrated that using glassy state of relaxor ferroelectrics above the Burns temperature can be instrumental in achieving very low thermal conductivity in these double perovskites to enhance the *ZT* values. Moreover, we discovered a new class of oxide materials exhibiting temperature driven p–n type resistance switching behavior coupled with a large change in thermopower, which can pave way for the fabrication of novel high temperature multifunctional devices.

II. DESIGN OF DOUBLE PEROVSKITES

Double perovskites have stoichiometric formula A$_2$B′B″O$_6$, where the B-sites, i.e., B′, B″ can be occupied by the different combination of transition metals.[42,43] The crystal structure and space group of double perovskites mainly depend on the arrangement of B′O$_6$ and B″O$_6$ octahedra, especially their ordering and tilting.[44] There are three types of B-site cationic arrangements in the 3-dimensional crystal structure, i.e., random, rock salt, and layered arrangement.[43] The space-group of double perovskites with randomly ordered octahedra is generally *Pm$\bar{3}$m*, as shown schematically in Fig. 1(a). In the unit cell of a randomly ordered (*Pm$\bar{3}$m*) double perovskite, the corner positions are occupied by A-site (0, 0, 0) divalent cations. However, B-site tetravalent cations (B′ and B″) are placed in the body centered position (1/2, 1/2, 1/2) and oxygen anions sit at the face-centered positions (1/2, 1/2, 0). On the contrary, in double perovskite structure with rock salt ordering, B′O$_6$ and B″O$_6$ octahedra are alternatively arranged in three-dimension space resulting different space groups, such as *Fm$\bar{3}$m*, *I4/m*, and *P4/nmc*. The least common crystal structure of the double perovskite is layered-type in which, the layers of B′O$_6$ and B″O$_6$ octahedra are alternately arranged only in one direction.

Over the years, various types of perovskite materials were designed based on the Goldschmidt tolerance factor.[45] Tolerance factor "*t*" is nearly 1 for cubic crystal structure. If the A-site cations have a smaller radius resulting in *t* < 1, cation size mismatch is generally compensated by tilting the BO$_6$ octahedra. However, if *t* > 1, due to the larger radius of A-site ion, the mismatch is not offset by octahedral tilting, and a hexagonal phase may form. The equation for tolerance factor[43] was further modified for our double perovskite structure, A$_x$′A$_{2-x}$B′B″O$_6$, where A′-cation was used as the dopant in the A-site. The modified equation for tolerance factor is given by the following equation:

$$t = \frac{\frac{(x)r_{A'} + (2-x)r_A}{2} + r_O}{\sqrt{2}\left(\frac{r_{B'} + r_{B''}}{2} + r_O\right)} \quad , \tag{2}$$

where, r_A, $r_{A'}$, $r_{B'}$, $r_{B''}$, and r_O are the ionic radii of ions.

TABLE I. TE properties such as electrical conductivity, Seebeck coefficient, power factor, and ZT of different oxide TE materials.

Composition	Crystal structure/ space group	Electrical conductivity (σ_{max})(S/m)	Seebeck coefficient (S_{max})(μV/K)	Power factor $(S^2\sigma_{max})$ (μW/mK^2)	ZT_{max}	Ref.
Double perovskites						
Sr$_2$YRuO$_6$	Monoclinic ($P2_1/n$)	4.5 (1150 K)	−475 (300 K)	~0.27 (1150 K)	...	13
Sr$_2$ErRuO$_6$	Monoclinic ($P2_1/n$)	9.09 (1150 K)	−400 (300 K)	~0.56 (1150 K)	0.025 (1250 K)	13
La$_2$CoRuO$_6$	Monoclinic ($P2_1/n$)	10 (300 K)	290 (400 K)	2.5 (1073 K)	...	14
La$_2$CrRhO$_6$	...	1.7 (300 K)	643.2 (300 K)	0.70 (300 K)	...	15
La$_2$CuRhO$_6$	...	1.7 × 10^3 (300 K)	149.5 (300 K)	39.4 (300 K)	...	15
Sr$_2$CoTiO$_6$	Tetragonal ($I4/m$)	1.3 × 10^3 (720 K)	120 (300 K)	4 (1230 K)	...	16
La$_{0.2}$Sr$_{1.8}$CoTiO$_6$	Tetragonal ($I4/m$)	2.6 × 10^3 (720 K)	70 (300 K)	3 (1230 K)	...	16
Ca$_2$FeMoO$_6$	Monoclinic ($P2_1/n$)	~10^5 (300 K)	~110 (1200 K)	350 (1200 K)	0.15 (1250 K)	17
Sr$_2$MnMoO$_6$	Monoclinic ($P2_1/n$)	183 (1220 K)	−368 (1240 K)	120 (1250 K)	0.13 (1100 K)	18
Ba$_{0.15}$Sr$_{1.85}$FeTiO$_6$	Cubic with ($Pm\bar{3}m$)	273 (900 K)	~680 (1123 K)	26 (1123 K)	...	19
Ba$_{0.15}$Sr$_{1.85}$Ti$_{0.8}$Fe$_{0.8}$Nb$_{0.4}$O$_6$	Cubic ($Pm\bar{3}m$)	~150 (930 K)	478 (935 K)	13 (930 K)	...	20
La$_{0.1}$Sr$_{0.9}$FeTiO$_6$	Cubic ($Pm\bar{3}m$)	510 (900 K)	−1282 (1188 K)	89.5 (1139)	...	21
Ba$_{0.2}$Sr$_{1.8}$TiCoO$_6$	Cubic ($Pm\bar{3}m$)	790 (1220 K)	328 (1220 K)	85 (1220 K)	0.3 (1220 K)	22
Bi$_{0.1}$Sr$_{1.9}$TiCoO$_6$	Cubic ($Pm\bar{3}m$)	3.8 × 10^3 (714 K)	106.5 (333 K)	5.7 (761 K)	...	23
Sr$_2$TiMoO$_6$	Cubic ($Pm\bar{3}m$)	1.3 × 10^5 (300 K)	−7.73 (1220 K)	7.8 (1220 K)	...	24
La$_{0.25}$Sr$_{1.75}$TiMoO$_6$ x = 0.25	Cubic ($Pm\bar{3}m$)	1.6 × 10^5 (500 K)	−4.44 (1220 K)	4.49 (700 K)	...	25
Ba$_2$TiMoO$_6$	Cubic ($Pm\bar{3}m$)	1.17 × 10^5 (700 K)	−15 (1220 K)	20.79 (1220 K)	...	26
Ba$_{0.1}$Sr$_{1.9}$TiFe$_{0.5}$Mo$_{0.5}$O$_6$	Cubic ($Pm\bar{3}m$)	6.4 × 10^3 (1220 K)	−73 (1220 K)	34.2 (1220 K)	...	27
Sr$_2$TiCo$_{0.5}$Mo$_{0.5}$O$_6$	Cubic ($Pm\bar{3}m$)	3.7 × 10^3 (1220 K)	−40.6 (1220 K)	6.1 (1220 K)	...	28
Sr$_2$CoMoO$_6$ (after annealing)	Tetragonal ($I4/m$)	2.3 × 10^3 (~473 K)	−210 (1173 K)	~45 (1173 K)	...	29
Perovskite						
SrTi$_{0.85}$Nb$_{0.15}$O$_3$	Cubic	~ 900 (1220 K)	~ −195 (1220 K)	35 (1220 K)	...	30
La doped SrTiO$_3$ (single crystal)	...	10^5 (300 K)	~ −294 (1050 K)	~7 × 10^2 (1050 K)	0.27 (1073 K)	31
Nb doped SrTiO$_3$ (single crystal)	...	3.5 × 10^4 (300 K)	~ −370 (1050 K)	~4 × 10^2 (1050 K)-	0.17 (1073 K)	31
Ca$_{0.8}$Lu$_{0.2}$MnO$_3$	Orthorhombic	1.6 × 10^4 (1100 K)	−122 (973 K)	2.6 × 10^2 (973 K)	0.16 (973 K)	32
La$_{0.6}$K$_{0.4}$TiO$_3$	Cubic ($Pm\bar{3}m$)	3.2 × 10^4 (520 K)	−150 (850 K)	6 × 10^2 (720 K)	0.18 (800 K)	33
Nonperovskite oxides						
Ca$_{2.8}$Lu$_{0.2}$Co$_4$O$_{9+\ddot{o}}$	Layered cobaltite	1 × 10^4 (1200 K)	195 (1045 K)	4 × 10^2 (1070 K)	0.35 (1070 K)	34
BaAgCa$_{2.8}$Co$_4$O$_9$	Layered cobaltite	1.3 × 10^4 (1000 K)	171 (1000 K)	3.8 × 10^2 (1000 K)	0.3 (1000 K)	35

To design the materials' composition and dopant percentage, the tolerance factor [Eq. (2)] was calculated for Sr$_2$TiMO$_6$ double perovskites, where M = Fe, Co, and Mo. Tolerance factors with respect to the percentages of 'A'-site doping for these double perovskite systems are plotted in Fig. 1(b). It is evident from the figure that pure Sr$_2$TiCoO$_6$ (STC) shows higher tolerance factor than Sr$_2$TiMoO$_6$ (STM) and Sr$_2$TiFeO$_6$ (STF) ceramics. Tolerance factor 't' was found to increase with the substitution of Ba for the Sr-site in all the double perovskites such as STC, STF, and STM, whereas 't' decreased with the La doping. Nevertheless, the tolerance factor values for all the compositions developed in the present work found to be within the range of 1 ± 0.03. It predicts that

SrTiO$_3$-based double perovskites are stable with a cubic crystal structure.

III. PROCESSING OF DOUBLE PEROVSKITES

In general, double perovskites are electrical insulators. However, in the TE applications, very good electrical conductivity of the material is desired. To engineer double perovskite oxides with reasonable electrical conductivity, it is essential to attain a single phase solid solution. The presence of impurities or secondary phase deteriorates the electrical conductivity. We used the solid-state reaction method in the present work to prepare solid solution of double perovskites. This method
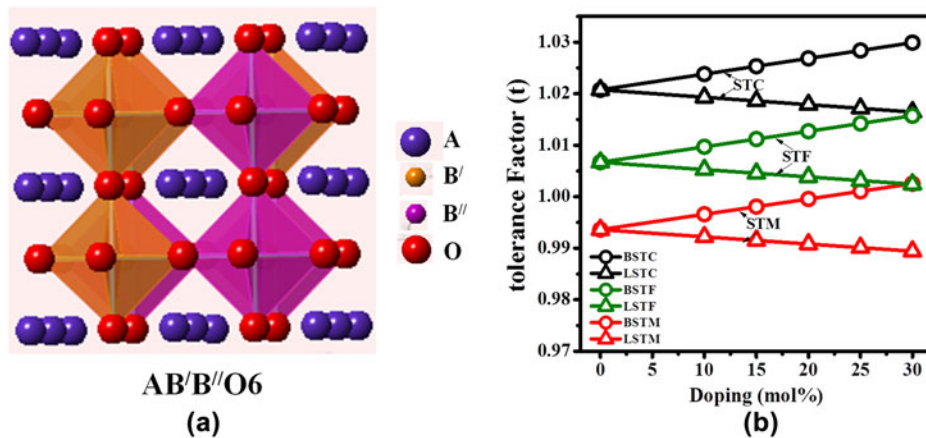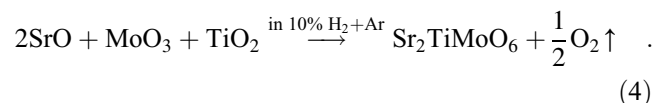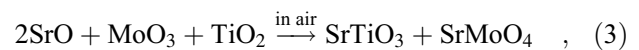
FIG. 1. (a) Schematic of A$_2$B′B″O$_6$ double perovskite structure and (b) tolerance factor of Ba and La-doped Sr$_2$TiCoO$_6$ (STC), Sr$_2$TiFeO$_6$ (STF), and Sr$_2$TiMoO$_6$ (STM).

includes calcination of a homogeneous mixture of different powders such as oxides, carbonates, etc. This solid-state reaction process contains repeated grinding, milling, and sintering at high temperature. During sintering and calcination, various parameters such as temperature, heating/cooling rate, gas flow, etc. were optimized to acquire the required resultant phase of ceramic materials. There was another important step that we included in the current work, i.e., nanomilling of calcined powder. After nanomilling, the particle size of the starting powder for sintering was reduced to <100 nm. Smaller particle size is important to achieve the small grain size in the microstructure of the sample, which can enhance the phonon scattering at grain boundaries resulting in low lattice thermal conductivity (κ_l) of the ceramic materials. The calcined powder was milled by planetary micromill (Fritsch, PULVERISETTE 7 premium line, Rhineland Palatinate, Germany) at 600 rpm using zirconia grinding balls and ethanol as milling media. The schematic of the processing steps involved in the fabrication of double perovskite ceramics by the solid-state reaction method is presented in Fig. 2.

A. Effect of processing atmosphere

To obtain good electrical conductivity, we used transition metals with multiple oxidation states in the B-site of the double perovskite, which has the formal valence of +4. Hence, unwanted secondary phases might form in the system. In calcination and sintering, the processing atmosphere, i.e., inert (Ar, N$_2$), oxidizing (Air) and reducing (H$_2$) play a significant role in the formation of a single phase. Initially, we calcined and sintered La- and Ba-doped Sr$_2$TiMoO$_6$ in air. To analyze the phase purity and crystal structure of calcined and sintered sample, X-ray diffraction (XRD) was carried out by using a PAN-analytical Empyrean ACMS 101 (Malvern Panalytical Ltd., Malvern, United Kingdom) diffractometer at room temperature. The XRD pattern of calcined and sintered powder showed that solid state reactions were not completed in air. We found a secondary phase, SrMoO$_4$, as confirmed by the XRD profile in Fig. 3(a). SrMoO$_4$ phase segregation suggests that Mo is more stable with +6 oxidation state as depicted by Eq. (3). The SrMoO$_4$ phase exhibits insulating behavior and significantly reduces the overall conductivity of the system. However, Mo has a formal valence of (+4) in the double perovskite structure. To troubleshoot this problem, repeated process of grinding followed by calcination was carried out in reducing atmosphere as described by Eq. (4). Single-phase solid solution was achieved when calcination and sintering were carried out in reducing atmosphere, as shown in Fig. 3(a). To the best of our knowledge, there was no report on STM-based double perovskites demonstrating single-phase solid solution. Therefore, the sintering temperature, as well as the atmosphere, played significant role in the fabrication of these double perovskites.

$$2SrO + MoO_3 + TiO_2 \xrightarrow{\text{in air}} SrTiO_3 + SrMoO_4 \quad , \quad (3)$$

$$2SrO + MoO_3 + TiO_2 \xrightarrow{\text{in 10\% H}_2 + \text{Ar}} Sr_2TiMoO_6 + \frac{1}{2}O_2 \uparrow \quad . \quad (4)$$

To determine the crystal structure of double perovskite oxides, Rietveld refinement of room temperature powder XRD data was carried out using Full Prof Program[46] for all the double perovskite samples. We obtained a single-phase cubic symmetry for all the SrTiMO$_6$ double perovskites, where M = Co, Mo, and Fe. The observed (open circle), calculated (continuous line), and the difference profiles obtained after refinement of the XRD pattern of LSTM $x = 0.1$ are shown in Fig. 3(b). The
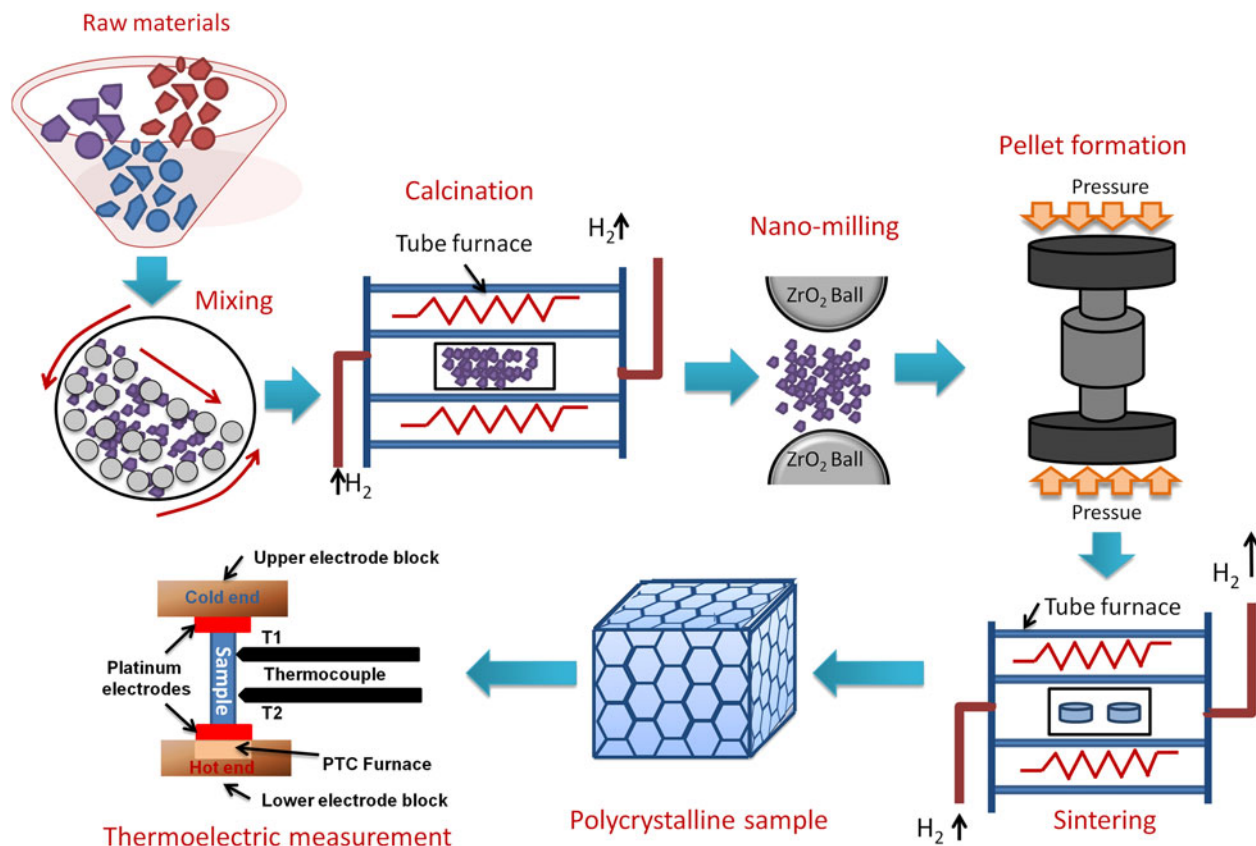
FIG. 2. Schematic of processing double perovskite ceramics by the solid-state reaction method and its TE measurement.

XRD data show a well-fitted graph with respect to $Pm\bar{3}m$ space group with very low-value of χ^2 (1.41), which signifies the goodness of fit in the Rietveld refinement.[25]

The microstructure of all the ceramic samples (~95–97% density) was analyzed by scanning electron microscopy (SEM) (Carl Zeiss GmbH, EV050, Oberkochen, Germany). All the double perovskite ceramic samples showed well-sintered, dense microstructure, as shown in Fig. 3(c) for LSTM.[25] These double perovskites demonstrated a wide range of grain size distribution scaling from nm to μm range. Due to nanoscale high energy ball milling of calcined powder, we obtained a significant amount of grain size <500 nm reduction.

B. Effect of annealing

We studied the effect of annealing on the TE properties of Sr_2CoMoO_6-based double perovskite oxide.[29] Figure 4 shows the structural and TE properties of as-sintered Sr_2CoMoO_6 (SCMO) oxide in comparison with SCMO sample annealed in reducing atmosphere. XRD of air-sintered SCMO implied the signature of a small concentration of nonperovskite phase $SrMoO_4$, as shown in Fig. 4(a). Furthermore, we carried out the Rietveld refinement using Fullprof program to reveal the crystal structure and weight percentage of Sr_2CoMoO_6 and

$SrMoO_4$ phase of the air sintered sample. The Sr_2CoMoO_6 and $SrMoO_4$ were fitted with $I4/m$ and $I4/a$ space group, respectively. However, the amount of this $SrMoO_4$ secondary phase was found to be 8.9 wt%. To reduce the amount of the $SrMoO_4$ phase, heat treatment was carried out in reducing atmosphere at 1273 K for 2 h. After annealing, there was an absence of $SrMoO_4$ phase, as shown in Fig. 4(b). However, the extra peaks corresponding to the $SrMoO_3$ perovskite phase was also recorded. The annealing process not only changed the phase of the system but also showed the effect on the microstructure of SCMO ceramic. Before annealing, all the grains were distinguished with clearly defined grain boundaries, as shown in Fig. 4(c). However, the microstructure of SCMO after annealing demonstrated molten phase with micron-scale grain.[29]

Annealing of SCMO ceramic in reducing atmosphere affected its TE properties significantly. Air-sintered SCMO ceramic exhibited insulator like behavior up to 913 K (~0.2 S/m at room temperature) with p-type Seebeck coefficient, as shown in Fig. 4(e). Around 913 K, a sharp decrease in the Seebeck coefficient (S) was found and SCMO showed p–n type transition depicted in Fig. 4(e). After annealing, SCMO demonstrated n-type conduction behavior in the entire temperature range, as shown in Fig. 4(f). Furthermore, electrical conductivity was
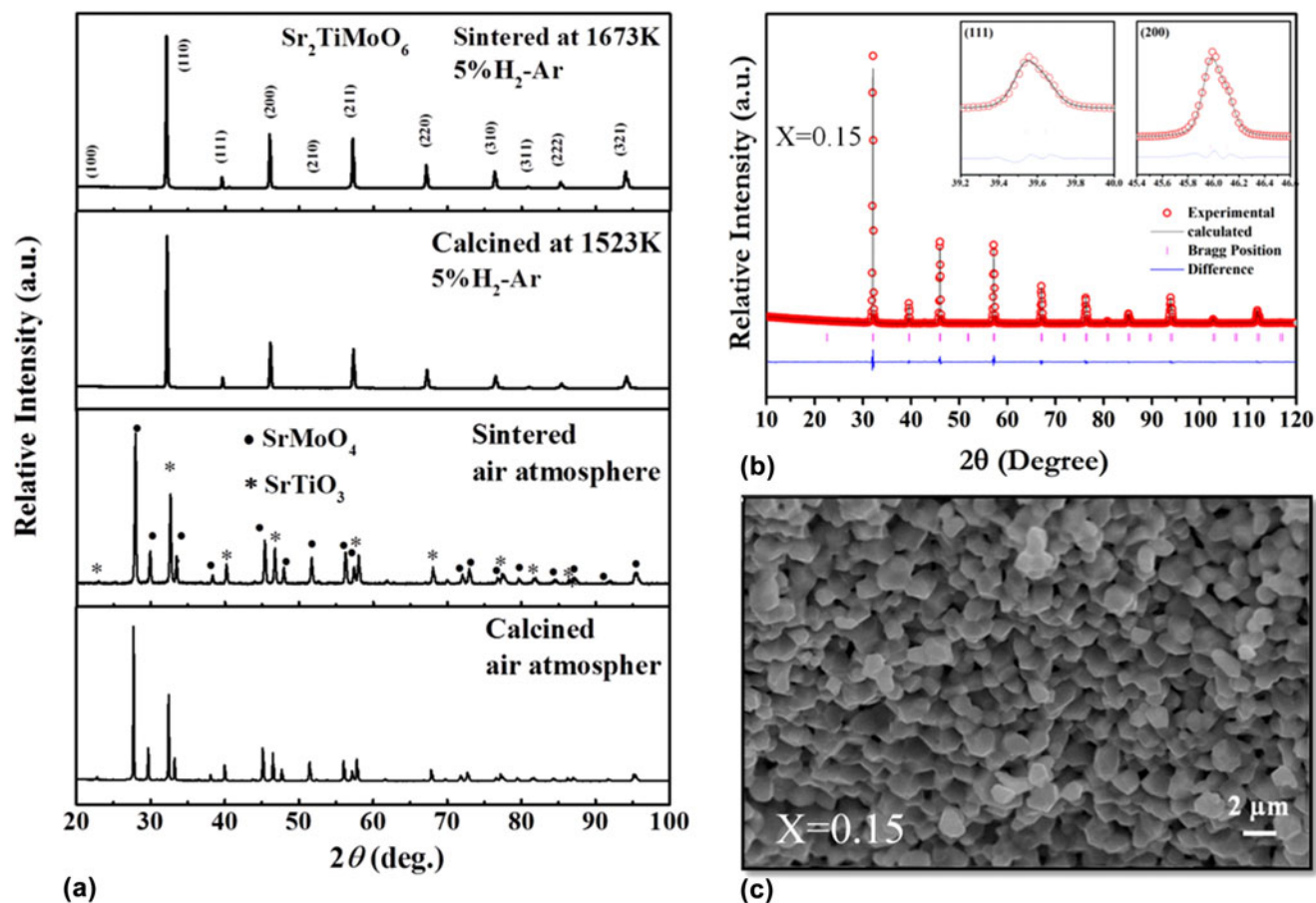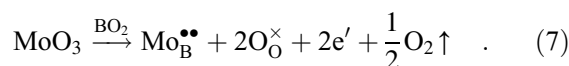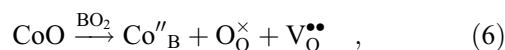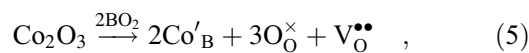
FIG. 3. (a) XRD pattern of STM powder calcined and sintered sample in the air and reducing atmospheres, (b) Rietveld analysis, and (c) SEM image of the fracture surface of the LSTM $x = 0.15$ ceramic sample. Reproduced from Ref. 25 with permission from The Royal Society of Chemistry.

enhanced by ten times after annealing. With increasing temperature, electrical conductivity was decreased indicating the metal-like behavior. The maximum power factor ($S^2\sigma$) value, ~45 μW/mK², was achieved at 1173 K, which is significantly higher as compared to air-sintered SCMO ceramics (~13 μW/mK² at 1173 K).[29] Hence, annealing was found to be an interesting way to enhance the electrical conductivity of any n-type TE materials and to improve the overall performance. The conduction mechanism of air-sintered and annealed sample was further explained by the following defect reactions:

$$Co_2O_3 \xrightarrow{2BO_2} 2Co'_B + 3O_O^\times + V_O^{\bullet\bullet} \quad , \quad (5)$$

$$CoO \xrightarrow{BO_2} Co''_B + O_O^\times + V_O^{\bullet\bullet} \quad , \quad (6)$$

$$MoO_3 \xrightarrow{BO_2} Mo_B^{\bullet\bullet} + 2O_O^\times + 2e' + \frac{1}{2}O_2\uparrow \quad . \quad (7)$$

The B-site cation in double perovskite oxides possesses formal valance of 4+. Hence, the B-site occupancy by Co^{3+} and Co^{2+} produces the oxygen vacancies

as expressed by defect reactions (5) and (6). These oxygen vacancies are the sources of the positive charge carriers in the SCMO sample. However, the presence of Mo^{6+} in SCMO donates negative charge carrier, electron as depicted by Eq. (7). Hence the presence of both low mobility oxygen vacancies and high mobility electrons are expected to exist in the SCMO system. The p-type conduction observed till 1023 K in the air-sintered sample suggests the presence of positively charged oxygen vacancies as majority charge carriers. The air-sintered sample showed the presence of $SrMoO_4$ as the secondary phase, which was reported as insulating in nature.[47] It validates the low electrical conductivity observed in the as-sintered sample. Moreover, at low temperature, electrons produced by defect reaction (7) are expected to be localized at defect sites in the ceramic sample. To overcome the energy barrier, the charge carriers (e^-) required the activation energy for delocalization. Small polaron hopping phenomena were found[29] to be the conductivity mechanism in SCMO. With increasing temperature, these electrons were expected to become delocalized contributing to the conductivity. The n-type conductivity observed in SCMO above 1023 K
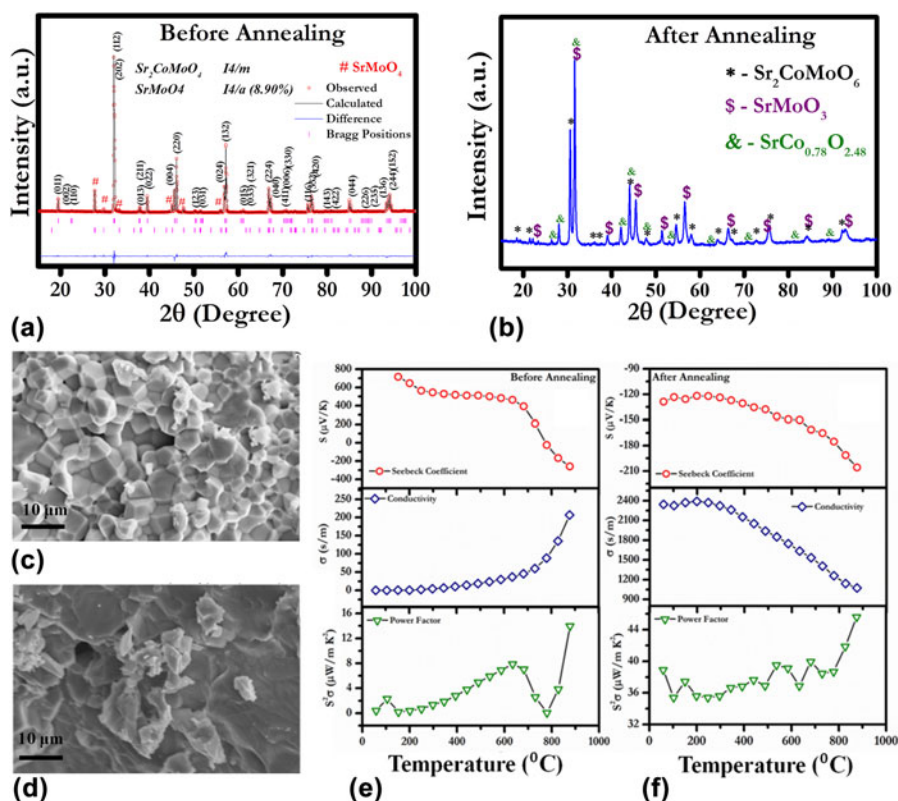
FIG. 4. (a) and (b) XRD, (c) and (d) SEM, (e) and (f) TE properties for SCMO ceramics before and after annealing, respectively. Reproduced from Ref. 29 with the permission of AIP Publishing.

suggests the high mobility electrons as majority charge carriers, which further corroborates the higher conductivity values obtained beyond 1023 K. On the other hand, the SrMoO$_3$ phase found in the annealed sample was reported to be metallic in nature.[48] As a result the annealed sample showed higher conductivity values as well as metal-like ($d\sigma/dT < 0$) behavior in the temperature-dependent conductivity plot, as shown in Fig. 4(f) unlike the air-sintered SCMO sample.

IV. LARGE THERMOPOWER IN DOUBLE PEROVSKITES

For the potential TE materials, it is essential to have a high thermopower ($S > 100$ μV/K) in combination with a high value of electrical conductivity resulting in high TE power factor ($S^2\sigma$). In the present work, we engineered the SrTiO$_3$-based double perovskite TE materials, Sr$_2$TiB′O$_6$, by using ferromagnetic elements (Co and Fe) at the B′-site, which resulted in double perovskites such as Sr$_2$CoTiO$_6$ (STC)[22] and Sr$_2$FeTiO$_6$ (STF).[19] Figure 5 shows the Seebeck coefficient and the electrical conductivity of these materials measured in the temperature range from 300 to 1200 K (ZEM-3 M10 apparatus, ADVANCE RIKO Inc., Yokohama, Japan). Both STF and STC compositions demonstrated positive Seebeck coefficient confirming the p-type behavior with holes as

the dominant charge carriers. The Seebeck coefficient of STF was found to be higher than STC composition.

Furthermore, we studied the effect of barium doping at A-site on TE properties of STC and STF. Doping of barium in the place of strontium increased the Seebeck coefficient of both STC and STF. Very large S value ~800 μV/K at 1100 K was obtained in the Ba$_{0.25}$Sr$_{1.75}$TiFeO$_6$ double perovskite. In the temperature-dependent conductivity curve, both STC and STF showed semiconductor ($d\sigma/dT > 0$) to metal-like ($d\sigma/dT < 0$) transition as evident in Figs. 5(a) and 5(d). Furthermore, the doping of Ba^{2+} at the Sr-site decreased the value of electrical conductivity in both STC and STF ceramics. Maximum conductivity value for STC was found to be higher than that of STF. The highest value of power factor ($S^2\sigma$) was found to be ~100 μW/mK^2 at 1200 K for Ba$_x$Sr$_{2-x}$TiCoO$_6$ with $x = 0.15$ composition. In the pure STC sample, two semiconductors to metal transition peaks were found at 700 K and 1170 K, respectively, unlike the STF sample as shown in Fig. 5(a). The first semiconductor to metal transition temperature ($T_{S–M}$) was found to be shifted to the higher temperature with the incorporation of Ba in the Sr-site. There could be a phase transition responsible for semiconductor to metal transition observed in STC. However, our laboratory scale high-temperature XRD did not show any peak splitting suggesting cubic phase in the whole temperature range of
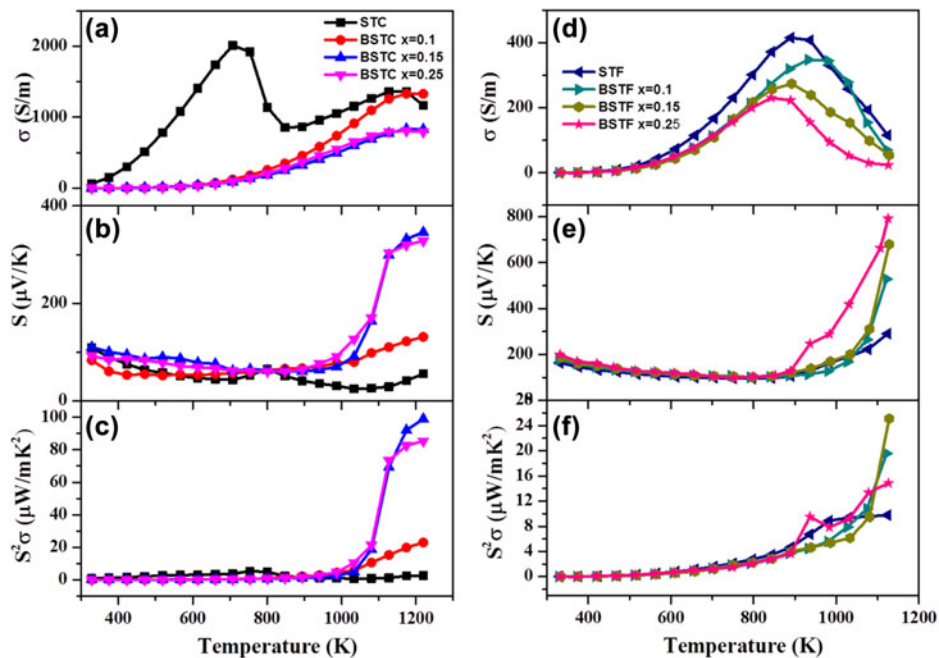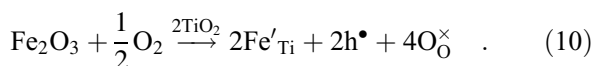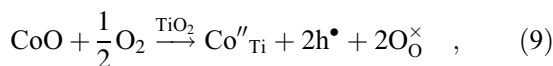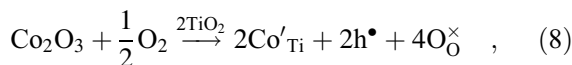
FIG. 5. TE properties such as (a) and (b) electrical conductivity, (c) and (d) Seebeck coefficient and (e) and (f) power factor of STC and STF-based TE materials. (a-c) reproduced from Ref. 22 with the permission of AIP Publishing and (d-f) reproduced from Ref. 19 with permission from The Royal Society of Chemistry.

measurement. High-resolution XRD or neutron diffraction is required to unravel the possible phase transition in the STC sample. It is to be noted that these materials exhibited relaxor ferroelectricity as discussed in the subsequent section of this manuscript. Hence it is difficult to solve the crystal structure of BSTC since the metal–semiconductor transition temperatures belonged to the paraelectric region, which is known to possess the cubic crystal structure. Hence one may need to resolve the local structural ordering in this system.

Majority charge carriers (holes, h•) in STC and STF-based double perovskites can be explained by the charge compensation mechanism due to the substitution of B-site having formal charge +4 with multivalent cations such as Fe and Co. Defect reactions can be expressed by using Kröger–Vink notation.

$$\text{Co}_2\text{O}_3 + \frac{1}{2}\text{O}_2 \xrightarrow{2\text{TiO}_2} 2\text{Co}'_{\text{Ti}} + 2\text{h}^{\bullet} + 4\text{O}_{\text{O}}^{\times} \quad , \quad (8)$$

$$\text{CoO} + \frac{1}{2}\text{O}_2 \xrightarrow{\text{TiO}_2} \text{Co}''_{\text{Ti}} + 2\text{h}^{\bullet} + 2\text{O}_{\text{O}}^{\times} \quad , \quad (9)$$

$$\text{Fe}_2\text{O}_3 + \frac{1}{2}\text{O}_2 \xrightarrow{2\text{TiO}_2} 2\text{Fe}'_{\text{Ti}} + 2\text{h}^{\bullet} + 4\text{O}_{\text{O}}^{\times} \quad . \quad (10)$$

Due to the substitution of isovalent Ba^{2+} in the place of Sr^{2+} ions, no changes in charge carrier dynamics was expected, which explains p-type behavior observed in all the BSTC and BSTF compositions.

However, the doping in A-site and B-site of double perovskite with metals having much higher oxidation state is expected to introduce e⁻s in these oxides. As a result, these double perovskites give rise to some new exciting behavior as discussed in a subsequent section.

V. DECOUPLING OF 'PHONON-GLASS' AND 'ELECTRON-CRYSTAL' BEHAVIOR IN OXIDES USING RELAXOR FERROELECTRIC INDUCED DIPOLAR SPIN GLASS

To achieve good ZT values in TE materials, it is essential to have high electrical conductivity and low thermal conductivity. It means that we need materials where electron transport in the medium should be as smooth as possible, but on the contrary, heat transport in the material should be as hard as possible. Slack summarized well this phenomenon by proposing "phonon glass electron crystal" model.[49] To determine the heat transport in the BSTC double perovskite, thermal diffusivity (D) and heat capacity (C_p) were measured in the temperature range from 300 to 1273 K. The formula $\kappa = \rho C_p D$ was used to calculate the thermal conductivity of these materials, where ρ is the density of samples. Thermal conductivity (κ) of all BSTC samples varies from 0.01 to 0.55 W/mK[22], as shown in Fig. 6(a). Lattice thermal conductivity (κ_l) of the system was calculated by subtracting electronic thermal conductivity (κ_e) from total thermal conductivity (κ). Electronic thermal conductivity

(κ_e) was calculated by using Wiedemann–Franz law, $\kappa_e = LT\sigma$, where L is the Lorentz number, σ is the electrical conductivity, and T is the temperature. Figure 6(b) shows the lattice thermal conductivity of BSTC ceramics. However, electronic thermal conductivity (κ_e) was found to be very small in this BSTC system. Thus, thermal conductivity of BSTC ceramics is primarily controlled by phonon transport (lattice thermal conductivity). Such glass-like low thermal conductivity is very beneficial to increase the figure of merit (ZT) and the performance of the TE device. The maximum value of ZT was obtained as ~0.3 at 1220 K in BSTC with $x = 0.2$ composition, as shown in Fig. 6(c).

However, the origin of such glass-like thermal conductivity in these BSTC double perovskites could not be explained by just considering phonon scattering due to small grain size and multiple cation sites. Moreover, the thermal conductivity of the BSTC sample was found to be continuously increasing with temperature till 1200 K, as shown in Fig. 6. This is opposite to what was observed for other TE materials, which showed a decrease in thermal conductivity with increase in temperature.[13,17,50,51] However, the similar behavior of increasing thermal conductivity with temperature was found in the literature for the spin glass system.[52,53] Interestingly, such thermal conductivity behavior was also reported in the relaxor ferroelectric material, which is known to behave like dipolar spin glass.[54]

Furthermore, we studied the dielectric behavior of BSTC ceramics to check if the material is relaxor indeed. The temperature dependence of dielectric constant (ε') and loss tangent (tan δ) at various frequencies for all the BSTC compositions in the temperature range from 100 to 350 K is shown in Fig. 6(d). These materials showed relaxor behavior at low temperature, i.e., with increasing frequency dielectric permittivity, ε' decreased and the temperature of dielectric maxima was shifted toward higher temperatures. Also, these BSTC compositions were found to follow the modified Curie–Weiss law as described by the following equation[55]:

$$\frac{1}{\varepsilon} - \frac{1}{\varepsilon_m} = \frac{(T - T_m)^{\gamma}}{C_1} \quad , \qquad (11)$$

where γ is called a degree of relaxation and its values lie between 1 and 2. The value $\gamma = 1$ shows that the Curie–Weiss law is valid for normal ferroelectric behavior. However, $\gamma = 2$ expresses the case of quadratic dependence suitable for an ideal relaxor ferroelectric.[56] The γ value obtained for this BSTC composition is 1.54, which suggests the ferroelectric relaxation behavior in these ceramics. Relaxor ferroelectrics are known to behave like dipolar glass[57,58] where dipolar interactions of polar nanoregions (PNR) are thought to be responsible for relaxor behavior. However, at very high temperature, thermal fluctuations are so large that there are no such
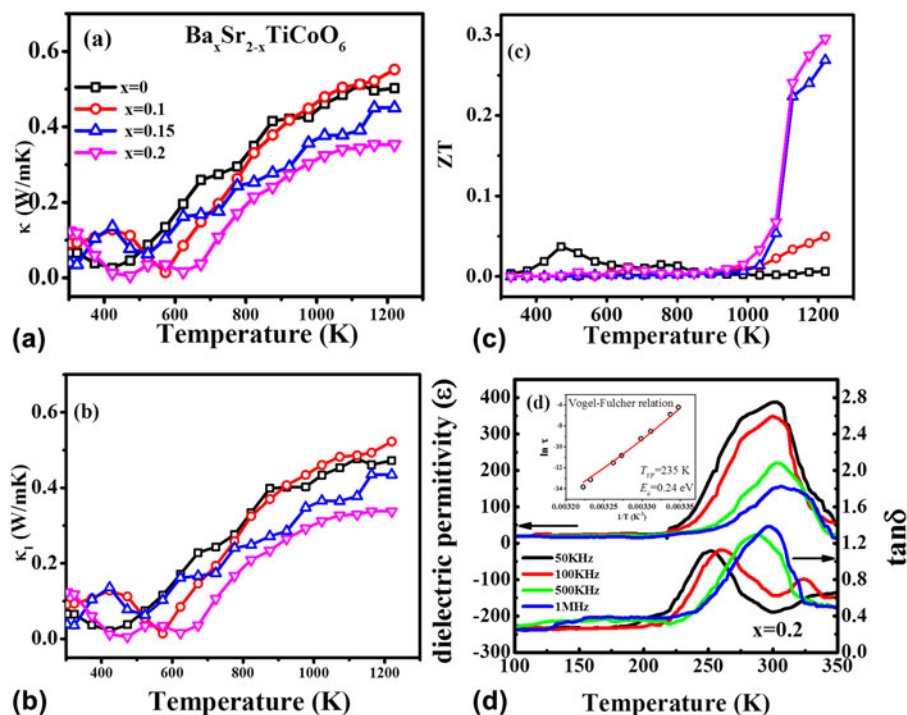

FIG. 6. Temperature dependence (a) thermal conductivity, (b) lattice thermal conductivity, (c) ZT of Ba$_x$Sr$_{2−x}$TiCoO$_6$ ceramics with $x = 0.0$, 0.1, 0.15, and 0.2, (d) dielectric constant (ε) and tan δ of Ba$_{0.2}$Sr$_{1.8}$TiCoO$_6$ ceramics and the inset shows the Vogel–Fulcher fitting. Reproduced from Ref. 22 with the permission of AIP Publishing.

well-defined dipole moments and it exhibits glass-like behavior above Burns temperature (T_D).[59–61] The Burns temperature (T_D) value for BSTC with $x = 0.2$ composition was calculated to be 312 K at 100 kHz, which suggests that BSTC double perovskite becomes a glassy state above 312 K. The relaxation time (τ) for these relaxors[62–64] can be estimated by Vogel–Fulcher law, which was originally derived for spin glass as described by the following equation:

$$\tau = \tau_0 \exp[E_a/k_B(T_m - T_{VF})] \quad , \qquad (12)$$

where τ_0 is the pre-exponential factor, E_a is the activation energy for polarization fluctuations of an isolated cluster, k_B is the Boltzmann constant, T_m is the temperature corresponding to dielectric maxima, and T_{VF} is the characteristic Vogel Fulcher freezing temperature. The temperature dependence of relaxation time of BSTC double perovskite was found to be well fitted with the Vogel Fulcher relation, as shown in the inset of Fig. 6(d) for Ba$_{0.2}$Sr$_{1.8}$TiCoO$_6$ composition. It further justifies that these double perovskites behave like spin glass as a result of relaxor ferroelectricity. Moreover, these relaxors above Burns temperature (T_D) behave like glass, which is the reason behind such low glass-like thermal conductivity observed in these double perovskite. Inducing dipolar glassy phase as a result of relaxor ferroelectricity in double perovskites can be a good strategy for decoupling

'Phonon-Glass' and 'Electron Crystal' behavior in oxides, which was considered as the bottleneck in the research of oxide TEs. Here we showed that using relaxor ferroelectrics above Burns temperature can produce glass-like thermal conductivity without affecting electrical conductivity much. To the best of our knowledge, this is the first material to demonstrate that decoupling of 'Phonon Glass' and 'Electron Crystal' behavior is possible in oxides.

Furthermore, we compared the thermal conductivity of BSTC double perovskites with wide range of oxides such as double perovskites, single perovskites, layered oxide-like Ruddlesden–Popper phases and nonperovskite oxides, as summarized in Table II. It is evident that the thermal conductivity of the BSTC samples was found to be comparable with some double perovskites. However, it demonstrated lower thermal conductivity compared to other layered perovskite and nonperovskites. The trend in temperature-dependent thermal conductivity of BSTC ceramics was found to be similar to that what was reported for the relaxors ferroelectrics and spin glasses.[54,65] However, we could not find any high-temperature studies on spin glasses as their thermal conductivity was studied primarily for other purposes such as magnetoresistance. Although some nonperovskite oxides showed a slightly increasing trend in thermal conductivity. However, there is no proper explanation for this behavior available in the literature. More theoretical

TABLE II. Thermal conductivity of different oxides.

Composition	Structure	Thermal conductivity (W/mK) at low temperature	Thermal conductivity (W/mK) at high temperature	Ref.
Ba$_{0.2}$Sr$_{1.8}$TiCoO$_6$		0.11 at 300 K	0.35 at 1220 K	22
Sr$_2$RuYO$_6$		~0.44 at 300 K	~0.22 at 1270 K	13
Sr$_2$RuErO$_6$		~0.30 at 300 K	~0.16 at 1270 K	13
Sr$_2$FeMoO$_6$	Double perovskite	~0.64 at 300 K	~0.20 at 1050 K	51
Sr$_{1.7}$Ba$_{0.3}$FeMoO$_6$		~0.76 at 300 K	~0.20 at 1050 K	51
Ca$_2$FeMoO$_6$		~4.1 at 300 K	~3.10 at 1020 K	17
Ca$_{1.7}$Sr$_{0.3}$FeMoO$_6$		~3.7 at 300 K	~2.2 at 1020 K	17
Pb$_2$FeMoO$_6$		~1.4 at 300 K	. . .	66
Pr$_{0.9}$Sr$_{0.1}$Mn$_{0.9}$Fe$_{0.1}$O$_3$		0.68 at 300 K	~0.94 at 1000 K	67
Ho$_{0.9}$Ca$_{0.1}$CoO$_3$		~0.85 at 350 K	~1.24 at 850 K	68
La$_{0.5}$Na$_{0.5}$Ti$_{0.8}$Nb$_{0.2}$O$_3$		2.1 at 300 K	2.5 at 950 K	69
La$_{0.6}$K$_{0.4}$TiO$_3$	Perovskite	2.45 at 300 K	2.36 at 950 K	33
Pb(Mg$_{1/3}$Nb$_{2/3}$)O$_3$ (relaxor ferroelectric)		~0.5 at 80 K	. . .	54
(Pb$_{0.915}$La$_{0.085}$) (Zr$_{0.65}$Ti$_{0.35}$)O$_3$ (relaxor ferroelectric)		~0.1 at 21 K	. . .	54
Pb(Mn$_{0.5}$Ta$_{0.5}$)O$_3$ (relaxor ferroelectric)		~0.08 at 15 K	. . .	54
Sr$_{0.65}$Ba$_{0.35}$Nb$_2$O$_6$ (relaxor ferroelectric)		~0.7 at 88 K1	. . .	54
Sr$_{1-x}$Ba$_x$(Nb$_2$O$_6$) $x = 0.55$ (relaxor ferroelectric)	Nonperovskite oxide	~0.8 at 70 K	. . .	65
Nd$_{1-x}$Sr$_{1+x}$CoO$_4$ $x = 0.33$ (layred cobalt oxide)		1.5 at 300 K	. . .	70
20%Nb doped SrO(SrTiO$_3$)		~5.0 at 300 K	~2 at 1000 K	71
(Sr$_{1-x}$La$_x$)$_{n+1}$Ti$_n$O$_{3+n}$ $x = 0.05$, $n = 2$	Ruddlesden-popper phases	~4.8 at 300 K	~2.58 at 1000 K	72
(Sr$_{1-x}$Eu$_x$)$_3$Ti$_2$O$_7$ $x = 0.05$		~4.20 at 300 K	~2.4 at 1000 K	73
SrO(SrTiO$_3$)$_n$ $n = 1$		~4.45 at 300 K	~1.9 at 1000 K	74

as well as experimental analyses are required to understand the heat transport behavior in these double perovskites.

VI. METAL-LIKE ELECTRICAL CONDUCTIVITY IN OXIDES

Both STC and STF materials discussed above showed good Seebeck coefficient. However, these materials suffered from low electrical conductivity ($\sim 10^2$ S/m) causing low power-factor obtained in these ceramics. Increasing the electrical conductivity of oxides is a daunting task because oxides are inherently insulator in nature. Recently, we developed Sr$_2$TiMoO$_6$ (STM)-based TE materials[24] which demonstrated metal-like electrical conductivity ($\sim 10^5$ S/m). We also studied the effect of lanthanum and barium doping on A$_x$Sr$_{2-x}$TiMoO$_6$ based TE materials. Figure 7 shows TE properties like electrical conductivity (σ), Seebeck coefficient (S), and power factor ($S^2\sigma$) of A$_x$Sr$_{2-x}$TiMoO$_6$ (A = La, Ba) ceramic samples in the temperature range from 300 to 1273 K. Very high carrier concentration on the order of 10^{22} cm^{-3} was found in the Hall measurement of these double perovskites. The highest value of electrical conductivity, 1.64×10^5 S/m, at 517 K was obtained for La$_{0.25}$Sr$_{1.75-}$TiMoO$_6$ composition, as shown in Fig. 7(a).

The Seebeck coefficient (S) of these materials showed temperature driven p-type to n-type conduction switching

behavior. However, the p–n type switching temperature was found to be decreased with increasing Ba concentration in BSTM composition in contrary to LSTM, where the p–n transition temperature was increased due to La doping, as shown in Fig. 7. In the n-type region, Seebeck coefficient (S) for all the compositions was found to be increased with temperature. Although these STM-based double perovskites showed metallic behavior ($d\sigma/dT < 0$) in the temperature-dependent conductivity graph, they were not found to follow the degenerate Fermi gas model in the Seebeck coefficient due to localized Anderson transition.[75,76] Generally, these kinds of perovskites with high carrier concentration ($>10^{18}$ cm^{-3}) are expected to show metal–insulator transition, as predicted by Mott criteria, $n_e^{1/3}a_0 \sim 0.25$, where n_e is the electronic carrier concentration and a_0 is the Bohr radius related with the carrier.[77] As per the Mott criterion if the value exceeds 0.25, the conduction mechanism transforms from semiconductor to metallic.[78] Since STM based double perovskites possess very high carrier concentration (10^{22} cm^{-3}), they are expected to exhibit metallic behavior satisfying Mott criterion. However these STM-based compounds comprise transition metals like Ti and Mo, which are known to exist in multiple oxidation states. As a result, there can be a significant variation in the local electric fields and lattice distortions causing random electric field around the defect sites, resulting the charge carriers in the system
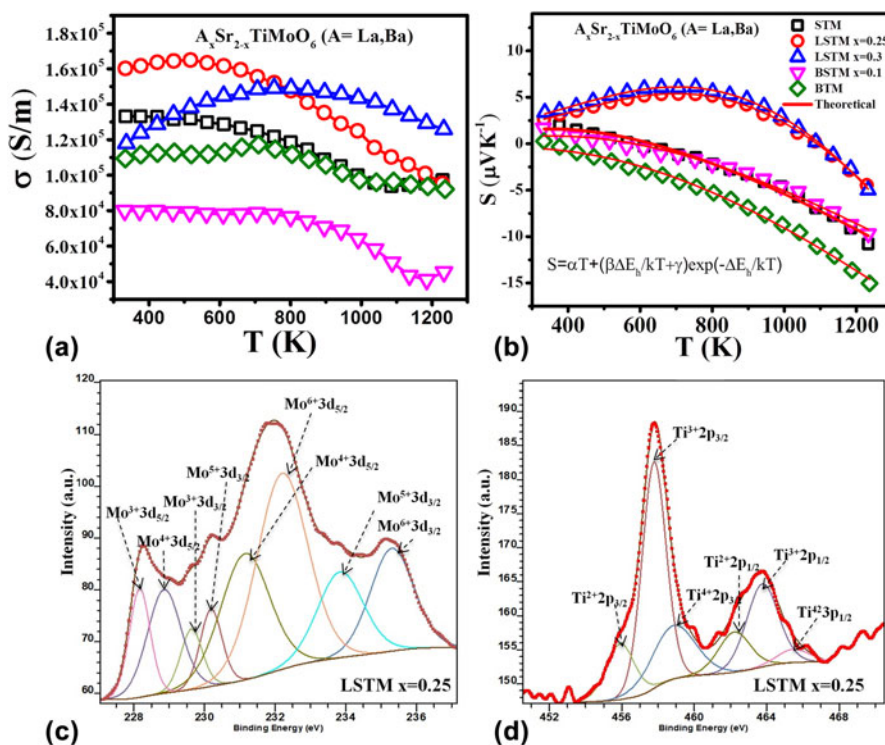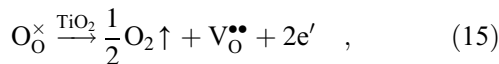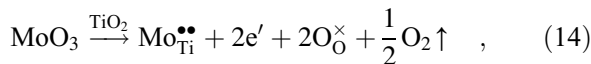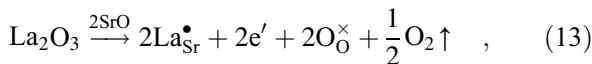

FIG. 7. TE properties: (a) electrical conductivity and (b) Seebeck coefficient of La- and Ba-doped STM ceramics with curve fitting and XPS analysis of (c) Mo and (d) Ti in LSTM with $x = 0.25$.

localized, which is known as Anderson localization.[75,76] As a result, these compounds do not follow the degenerate semiconductor model. To understand the charge transport mechanism in these complex oxides, it is essential to know the source of charge careers in these materials.

From the temperature-dependent Seebeck coefficient measurement of these samples showing p–n type switching, it is imperative to have the coexistence of both positive and negative charge carriers in these compounds. Source of negative charge carriers can be explained by defect reaction (13) and (14) which suggests that La^{+3} inclusion in the place of Sr^{+2} and Mo^{+6} in Ti^{+4} site are the reason behind the generation of electrons. Besides, the electron generation due to oxygen vacancies is inherent defect reaction in oxides especially at high temperature as depicted by Eq. (10). However, both Mo and Ti present in STM double perovskites can exist at +3 oxidation state as well. The cause of positive charge carriers in these materials was considered to be +3 oxidation state of Mo and Ti occupying B-site of the double perovskite, which has formal valence +4 as expressed by Eq. (16).

$$\text{La}_2\text{O}_3 \xrightarrow{2\text{SrO}} 2\text{La}^{\bullet}_{\text{Sr}} + 2\text{e}' + 2\text{O}^{\times}_{\text{O}} + \frac{1}{2}\text{O}_2\uparrow \quad , \quad (13)$$

$$\text{MoO}_3 \xrightarrow{\text{TiO}_2} \text{Mo}^{\bullet\bullet}_{\text{Ti}} + 2\text{e}' + 2\text{O}^{\times}_{\text{O}} + \frac{1}{2}\text{O}_2\uparrow \quad , \quad (14)$$

$$\text{O}^{\times}_{\text{O}} \xrightarrow{\text{TiO}_2} \frac{1}{2}\text{O}_2\uparrow + \text{V}^{\bullet\bullet}_{\text{O}} + 2\text{e}' \quad , \quad (15)$$

$$\text{M}_2\text{O}_3 \xrightarrow{2\text{TiO}_2} 2\text{M}'_{\text{Ti}} + \text{V}^{\bullet\bullet}_{\text{O}} + 3\text{O}^{\times}_{\text{O}} \quad , \quad (16)$$

where M = Mo, Ti.

Above defect reactions suggest that STM-based double perovskites can have the presence of electrons as well as positively charged oxygen vacancies. However, oxygen vacancies are known to have lower mobility as compared to electrons. Furthermore, the multiple oxidation states of Mo and Ti cations was confirmed by X-ray photoelectron spectroscopy (XPS; PHI 5000 Versaprobe II, ULVAC-PHI, Inc., Chigasaki, Japan) as shown in Figs. 7(c) and 7(d) for Mo 3d and Ti 2p spectra of LSTM $x = 0.25$. The XPS spectra confirmed the existence of Mo and Ti with multiple oxidation states. The obtained values of binding energies are very similar to the other reports in the literature.[79–82] XPS data suggest that the existence of Mo in +6 and +5 states enabled to reduce Ti even into +2 state, although in a little fraction of total Ti in the system. Mo^{3+}, Ti^{3+}, and Ti^{2+} were attributed to being the reason behind the positively charged oxygen vacancies. On the other hand, higher valence cations such as Mo^{5+} and Mo^{6+} generated the electrons.

Furthermore, we explained this p–n switching observed in the temperature-dependent Seebeck coefficient using an analytical model. In the case of coexisting electrons and holes, the total Seebeck coefficient 'S' was considered to be the sum of contribution from both types of charge carrier as given below.

$$S = (S^+\sigma^+ + S^-\sigma^-)/\sigma \quad . \quad (17)$$

Furthermore, the following equation can be derived:

$$S = \alpha T + (\beta\Delta E_\text{h}/kT + \gamma)\exp(-\Delta E_\text{h}/kT) \quad , \quad (18)$$

$$\text{where, } \alpha = \left(-\frac{\pi^2}{3}\right)\left(\frac{k^2}{e}\right)\left[\frac{1}{E_\text{F} - E_\text{C}}\right] \quad ,$$

$$\beta = \frac{\sigma_0 k}{Ae} \quad ,$$

$$\gamma = B\frac{\sigma_0 k}{Ae} \quad ,$$

where ΔE_h is the activation energy for generation of positive charge carriers, σ_0 and B are constant; k_B is the Boltzmann constant, e is a charge of the electron, T is the temperature, E_F is the Fermi energy, and E_C is the energy at the bottom of the conduction band. Detailed derivation of the proposed analytical model can be found in our earlier publication.[25] Figure 7(b) shows a least fitting curve for the temperature dependence of the Seebeck coefficient of STM-based ceramic samples by using Eq. (18). The proper fit to experimental data with our model [Eq. (18)] further validates that these samples have coexistence of high mobility electrons and low mobility oxygen vacancies. Nevertheless, these STM-based ceramic samples demonstrated that metal-like electrical conductivity ($\sim$10^5 S/m) is possible to attain in ceramics in the wide range of temperature from 300 to 1223 K.

VII. OPTIMIZATION OF POWER FACTOR BY COMPOSITIONAL MODIFICATION

The large Seebeck coefficient obtained in STC and STF-based double perovskites. However, these materials suffered from low electrical conductivity. On the other hand, we observed metal-like electrical conductivity (10^5 S/m) in Sr$_2$TiMoO$_6$-based double perovskite. However, their Seebeck coefficient is not very promising to be considered as good TE material.

Hence we further engineered a recipe of designing novel high-temperature TE materials by combining these two different types of double perovskites to use their respective good property coefficients, similar to what was used in composites over the years. However, in our case, two chosen materials have the same crystal structure and

similar lattice constant is resulting single-phase solid-solution. We investigated the TE properties of Sr$_2$Ti-Fe$_{0.5}$Mo$_{0.5}$O$_6$ (STFM), which can be considered as the combination of Sr$_2$TiFoO$_6$ having large Seebeck coefficient and Sr$_2$TiMoO$_6$ double perovskite, which exhibited metal-like electrical conductivity. Furthermore, we also synthesized Sr$_2$TiCo$_{0.5}$Mo$_{0.5}$O$_6$ (STCM), which can be regarded as the combination of Sr$_2$TiCoO$_6$ and Sr$_2$Ti-MoO$_6$ double perovskites.[28] These engineered double perovskite materials showed higher electrical conductivity as compared to Sr$_2$TiFeO$_6$ and Sr$_2$TiCoO$_6$. Besides, they demonstrated a negative Seebeck coefficient implying n-type TEs. Furthermore, we modified these materials by doping of Ba and La at Sr-site. Figure 8 shows the TE properties such as electrical conductivity, Seebeck coefficient and power factor of La$_x$Sr$_{2-x}$TiCo$_{0.5}$Mo$_{0.5}$O$_6$ (LSTCM) and Ba$_x$Sr$_2$TiFe$_{0.5}$Mo$_{0.5}$O$_6$ (BSTFM) ceramics. It can be seen from Fig. 8 that doping of La in the place of Sr in STCM increased the electrical conductivity but decreased the Seebeck coefficient. On the other hand, Ba-doping increased the Seebeck coefficient at the expense of the conductivity values in STFM. It shows that trade-off between the Seebeck coefficient and electrical conductivity can be done to achieve optimum power factor in these double perovskites by manipulating simply the doping concentration.

VIII. CHARGE TRANSPORT MECHANISM IN DOUBLE PEROVSKITES

In these types of transition metal-based perovskites, band model may not be a proper way to understand the conduction mechanism. In these materials, charge carriers are expected to be localized at defect sites. So activation energy should be required to overcome the energy barrier to

delocalize these carriers resulting in effective charge transport in the double perovskite. To explain the conduction mechanism, small polaron hopping conduction seems more suitable for these systems.[83–85] Equation (19) expressed the small polaron hopping conduction mechanism.[86]

$$\sigma = \frac{\sigma_0}{T} \exp\left[-\frac{E_{\text{Hop}}}{k_B T}\right] \quad , \qquad (19)$$

where E_{Hop} is the activation energy of polarons, T is the temperature, and k_B is the Boltzmann constant. If the small polaron hopping conduction is followed, then there should be a linear relation between ln (σT) and $1/k_B T$. Double perovskite oxides followed the small polaron hopping conduction mechanism in the semiconductor region of the conductivity curve as evident from the good linear fit shown in Fig. 9 for various double perovskite systems. Activation energy 'E_{Hop}' is equal to the slope of the curve between ln (σT) and $1/k_B T$. Table III presents the calculated E_{Hop} values for double perovskite oxides.

Thermopower is fundamentally a transport entropy of charge carrier that discloses the further information regarding charge transport mechanism. For these perovskite oxides in which small polaron hopping model drives conduction mechanism, thermopower can be explained by Heikes formula. Chaikin and Beni modified the formula to address the spin interactions of the electron better as given by the following equation[87]:

$$S = \frac{k_B}{e} \ln\left[\frac{2-c}{c}\right] \quad , \qquad (20)$$

where 'c' is the fractional small polaron concentration arising from multivalent cations occupying similar lattice
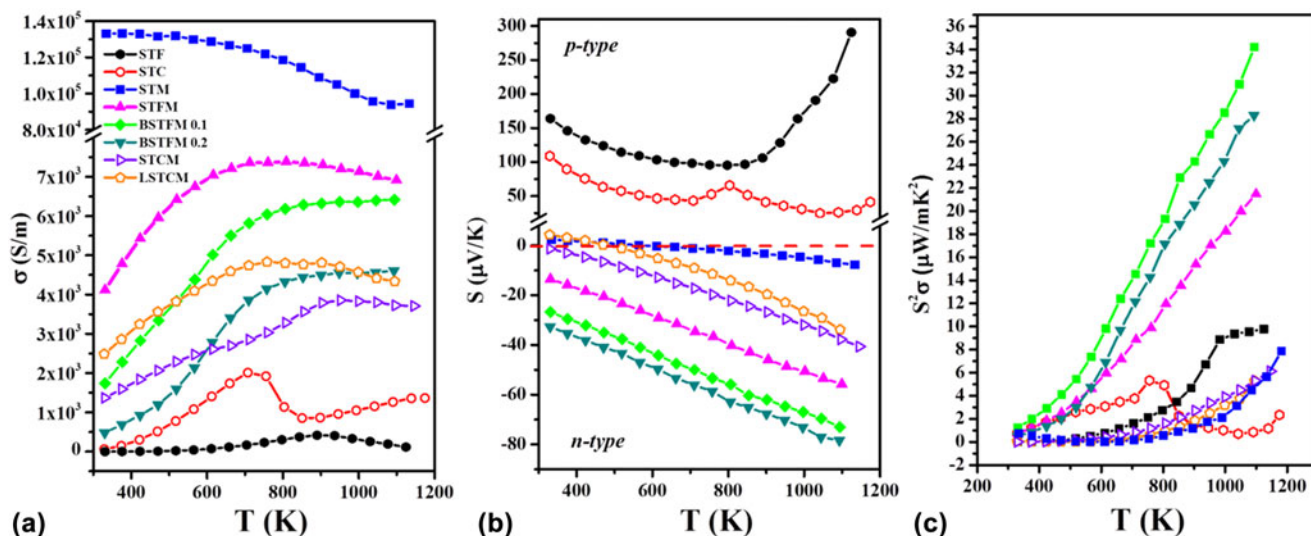

FIG. 8. TE properties: (a) electrical conductivity, (b) Seebeck coefficient, and (c) power factor of La and Ba doped STCM and STFM-based ceramics.

sites. Estimated values of c for double perovskite oxides are given in Table II. It is evident that as the activation energy decreases and the fractional polaron concentration, 'c' values increase in these double perovskites, the electrical conductivity of the material increases, which

further validates the proposed model for charge transport mechanism in these double perovskites.

IX. COLOSSAL CHANGE IN THERMOPOWER

Understanding the relationships between the structural and chemical compatibility, solid solubility, thermal stability, and lattice strain in perovskite structure can help in developing a broad range of novel functional materials. In modern electronics, development of novel inorganic semiconductor-based p–n junction has become pivotal for application in switches,[88] memory devices,[89] transistors,[90] sensors[91] etc.

In the current investigation, in the course of searching n-type oxide TE materials, we developed some novel SrTiO$_3$-based double perovskites, such as Ba$_x$Sr$_{2-x}$Ti$_{0.8}$Fe$_{0.8}$Nb$_{0.4}$O$_6$ (BSTFN), and La$_x$Sr$_{2-x}$TiFeO$_6$ (LSTF) which exhibited metal–semiconductor transition induced p–n type conduction switching with colossal change in thermopower. These BSTFN and LSTF ceramics were synthesized by the solid-state method with different amounts of Ba and La in the Sr site of Sr$_2$TiFeO$_6$-based double perovskites. Both the compositions, BSTFN and LSTF, exhibited semiconductor ($d\sigma/dT > 0$) to metal-like ($d\sigma/dT < 0$) transition and temperature driven p–n type conduction switching with enormous change in thermopower, as shown in Fig. 10. Also, the variation of thermopower of these double perovskites is depicted in Table IV.

The conduction switching of these compositions was first tried to be understood by the source of charge carriers. The source of positive charge carriers in Sr$_2$TiFeO$_6$ (STF) was explained by defect reaction expressed by Eq. (10) using Kroger Vink notation, where the substitution of Ti^{4+} ion with Fe^{3+} gave rise to holes as
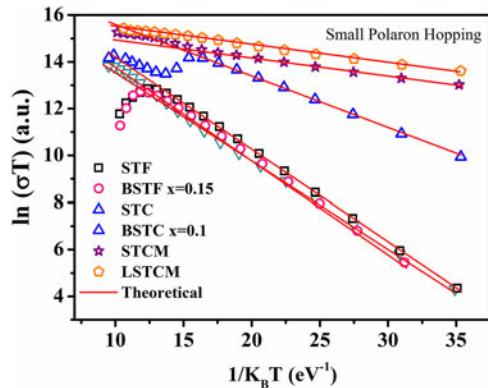

FIG. 9. Small polaron hopping (SPH) fitting of electrical conductivity of different double perovskite ceramic samples.

TABLE III. The calculated value of E_{Hop} required for generation of the charge carrier.

Compositions	E_{Hop} (eV)	Fractional small polaron concentration (c)	Electrical conductivity (S/m)
STF	0.393	0.26	400
BSTF $x = 0.1$	0.396	0.23	347
STC	0.226	0.71	2011
BSTC $x = 0.15$	0.380	0.48	834
STCM	0.08	0.99	3791
LSTCM	0.075	0.97	4608

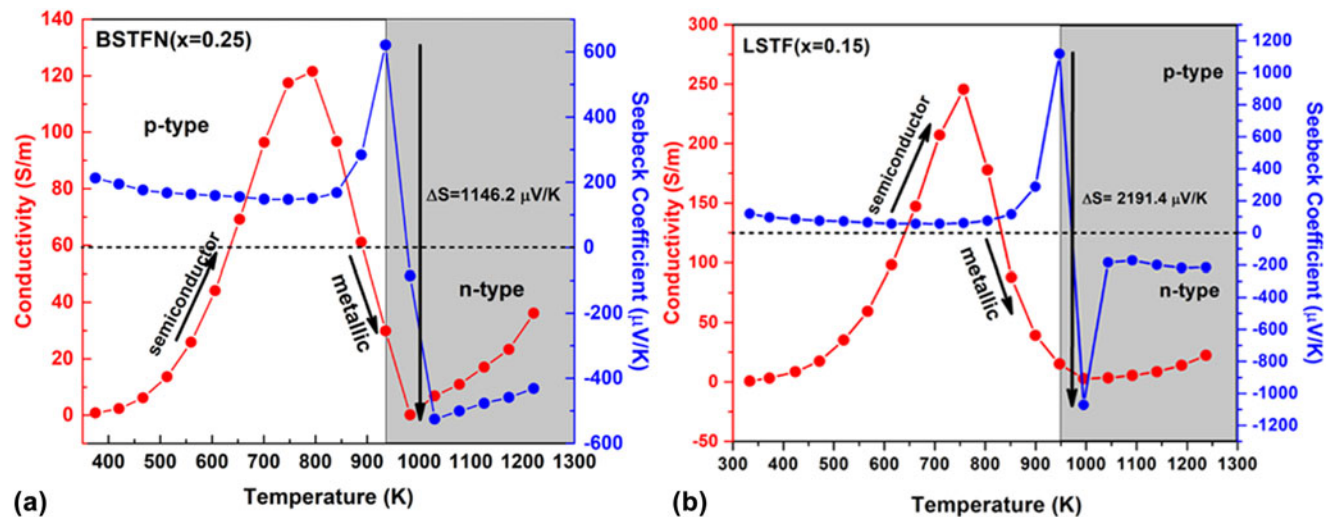FIG. 10. The electrical conductivity and thermopower variation with temperature for (a) BSTFN ($x = 025$) and (b) LSTF ($x = 0.15$) double perovskites. Reproduced from Ref. 20 with permission from PCCP Owner Societies.

majority charge carriers. The n-type behavior of the Sr$_2$Ti$_{0.8}$Fe$_{0.8}$Nb$_{0.4}$O$_6$ (STFN) ceramics at higher temperature arose due to the doping of Nb^{5+} in the place of Ti^{4+} ion at the B-site of the double perovskite structure as expressed by Eq. (21), suggesting electrons as the charge carriers.

$$Nb_2O_5 \xrightarrow{2TiO_2} 2Nb_{Ti}^{\bullet} + 2e' + 4O_O^{\times} + \frac{1}{2}O_2\uparrow \quad . \quad (21)$$
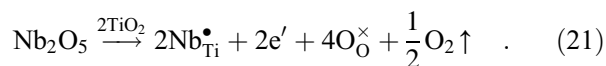
To verify the oxidation state of the B site cations, we further performed X-ray photoelectron spectroscopy of the BSTFN compositions and it confirms the presence of Fe in 3+ and 2+ states,[92,93] Nb in 5+ and 4+ states[94,95] and Ti in 4+ & 3+ states,[96,97] as shown in Figs. 11(a)–11(c), respectively.

It is clear from the XPS analysis that pure STF, which behaved previously as a p-type semiconductor exhibited conduction switching (p to n-type) due to the incorporation of Nb in the B site of these double perovskite. Similarly, the n-type behavior of LSTF double perovskites can be described by Eqs. (13) and (15) and it is apparent that both electrons and holes are present in the BSTFN and LSTF systems. Hence the thermopower was

compensated by both types of charge carriers resulting in low values of S at room temperature, where it does not produce much electrical conductivity. However, the holes contributed by defect reaction Eq. (10) act as the dominant source of charge carriers from room temperature up to T_{p-n}, resulting in a positive thermopower value in the S versus T graph in both the ceramics, whereas beyond T_{p-n}, Eqs. (13), (15), and (21) dominated the conductivity behavior of these samples. The dominant defect reactions determine the major carriers in the system. Nevertheless, in these double perovskite systems, a p-type-to-n-type semiconductor phase transformation occurred via an intermediate metallic phase. Hence, it was hypothesized that p–n-type switching facilitated large electron restructuring in LSTF and BSTFN, which was responsible for colossal change in thermopower. Further investigation to trap those structural changes in high temperature XRD is currently underway.

Previously such p–n type conduction switching assisted large change in thermopower was reported in the literature for few chalcogenide-based compounds, only in the last five years. But for the very first time it was observed in perovskite-based oxide materials and also the change in thermopower was larger than the previously reported results, as shown in the comparison[20,21,98–102] bar chart in Fig. 12. Such p–n switching coupled with a large change in thermopower in a single material as a result of only temperature change, opens up a new avenue for developing novel high-temperature diodes, thyristors, sensors, switches, thermistors, etc. The target areas for these devices are envisaged in space, chemical plants, automobile industries, and consumer electronics like cell phones, in which overheating or overcharging can cause the explosion of batteries due to thermal runaway. Colossal change in thermopower on the order of a few millivolts per Kelvin, integrated with p–n-type conduction switching, may lead to the development of novel thermal runaway monitors. Moreover, it can also be used for chemical-to-thermal-to-electrical energy conversion on the

TABLE IV. Change in thermopower and its corresponding temperature obtained from the temperature-dependent thermopower graph for BSTFN and LSTF ceramics.

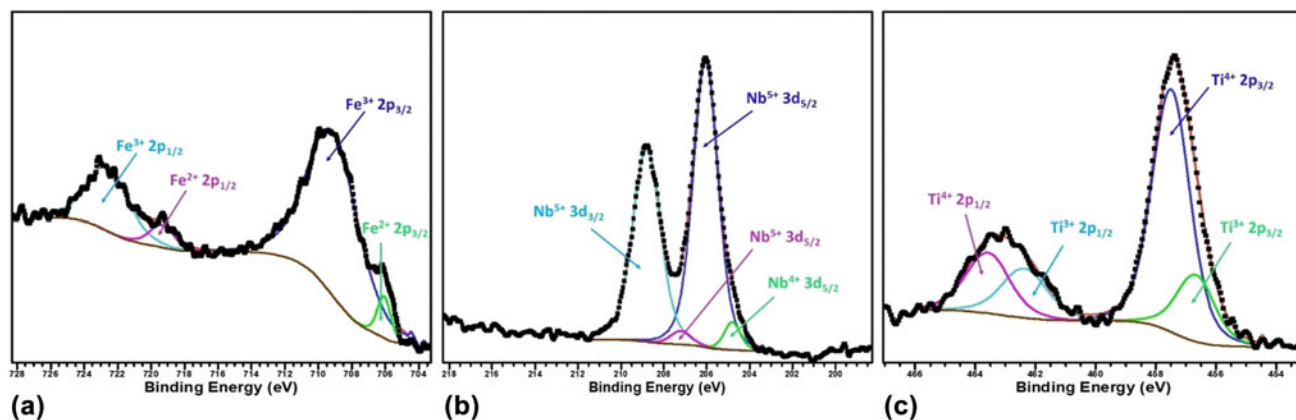| Composition (x)	Change in thermopower (ΔS) (μV/K)	Temperature of p–n switching (T_{p-n}) (K)
BSTFN 0.0	625	940.6
0.1	718.2	1035.6
0.15	988.8	983.1
0.25	1146.2	935.3
LSTF 0.1	2516.0	1139.9
0.15	2191.4	947.2
0.2	1342.0	941.8
0.25	1163.6	942.7

FIG. 11. The respective binding energy of Fe, Nb, and Ti in BSTFN double perovskite obtained by X-ray photoelectron spectroscopy.
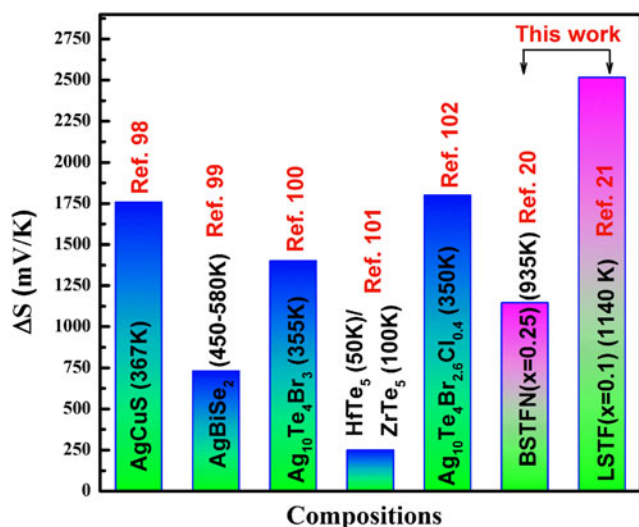
FIG. 12. Comparison of the maximum change in thermopower (ΔS) coupled with p–n type resistance switching behavior observed in different materials.

basis of the recently developed thermopower wave concept.

X. CONCLUSION

In the current work, a wide range of double perovskite oxide-based high-temperature TE materials were synthesized by the solid-state reaction method. The crystal structure of these materials was found to be cubic with $Pm\bar{3}m$ space group. A dense microstructure structure with grain size distribution scaling from nm to μm range was achieved in these double perovskites. It was shown that by manipulating cations and processing parameters, one can optimize electrical conductivity and Seebeck coefficient in these double perovskite oxides to achieve very good TE power factor. However, shift in semiconductor to metal transition temperature, T$_{S-M}$ by the doping played a key role in determining the operational temperature of these TE materials with maximum ZT values. Some of these double perovskites oxides also demonstrated temperature driven p–n switching assisted colossal change in Seebeck coefficient, which can be used for developing novel multifunctional devices. Conduction mechanism of these materials was explained by the small polaron hopping model. These double perovskites also showed low-temperature relaxor ferroelectric behavior inducing dipolar glassy phase. We demonstrated that using these relaxors above the Burns temperature, one can use the glassy phase of relaxor to obtain very low thermal conductivity without affecting its electrical conductivity. In other words, inducing glassy phase as a result of relaxor ferroelectricity in double perovskites can be a right approach for decoupling "Phonon-Glass Electron Crystal" behavior in these oxides. Nevertheless,

ZT values of these oxides are lower compared to that of chalcogenides and intermetallics, although oxides showed good thermal stability at high temperature. More efforts are needed to improve the ZT values of these double perovskite oxides to realize the commercialization of these materials for TE power generation.

ACKNOWLEDGMENT

REFERENCES

1. J. He, M.G. Kanatzidis, and V.P. Dravid: High performance bulk thermoelectrics via a panoscopic approach. *Mater. Today* **16**, 166 (2013).
2. R. Ovik, B. Long, M. Barma, M. Riaz, M. Sabri, S. Said, and R. Saidur: A review on nanostructures of high-temperature thermoelectric materials for waste heat recovery. *Renewable Sustainable Energy Rev.* **64**, 635 (2016).
3. K. Ullah, R. Saidur, H. Ping, R. Akikur, and N. Shuvo: A review of solar thermal refrigeration and cooling methods. *Renewable Sustainable Energy Rev.* **24**, 499 (2013).
4. S.F. Tie and C.W. Tan: A review of energy sources and energy management system in electric vehicles. *Renewable Sustainable Energy Rev.* **20**, 82 (2013).
5. M. Scheele, N. Oeschler, K. Meier, A. Kornowski, C. Klinke, and H. Weller: Synthesis and thermoelectric characterization of Bi$_2$Te$_3$ nanoparticles advanced. *Funct. Mater.* **19**, 3476 (2009).
6. B. Poudel, Q. Hao, Y. Ma, Y. Lan, A. Minnich, B. Yu, X. Yan, D. Wang, A. Muto, and D. Vashaee: High-thermoelectric performance of nanostructured bismuth antimony telluride bulk alloys. *Science* **320**, 634 (2008).
7. T. Caillat, J-P. Fleurial, and A. Borshchevsky: Preparation and thermoelectric properties of semiconducting Zn$_4$Sb$_3$. *J. Phys. Chem. Solids* **58**, 1119 (1997).
8. K. Kadel, L. Kumari, W. Li, J.Y. Huang, and P.P. Provencio: Synthesis and thermoelectric properties of Bi$_2$Se$_3$ nanostructures. *Nanoscale Res. Lett.* **6**, 1 (2011).
9. R. Brebrick and A. Strauss: Anomalous thermoelectric power as evidence for two-valence bands in SnTe. *Phys. Rev.* **131**, 104 (1963).
10. T. Takeuchi, T. Kondo, T. Takami, H. Takahashi, H. Ikuta, U. Mizutani, K. Soda, R. Funahashi, M. Shikano, and M. Mikami: Contribution of electronic structure to the large thermoelectric power in layered cobalt oxides. *Phys. Rev. B* **69**, 125410 (2004).
11. N. Van Nong, N. Pryds, S. Linderoth, and M. Ohtaki: Enhancement of the thermoelectric performance of p-type layered oxide Ca$_3$Co$_4$O$_9$ + δ through heavy doping and metallic nanoinclusions. *Adv. Mater.* **23**, 2484 (2011).
12. G.J. Snyder and E.S. Toberer: Complex thermoelectric materials. *Nat. Mater.* **7**, 105 (2008).
13. M.H. Aguirre, D. Logvinovich, L. Bocher, R. Robert, S.G. Ebbinghaus, and A. Weidenkaff: High-temperature thermoelectric properties of Sr$_2$RuYO$_6$ and Sr$_2$RuErO$_6$ double perovskites influenced by structure and microstructure. *Acta Mater.* **57**, 108 (2009).
14. T. Kawano, J. Takahashi, T. Yamada, and H. Yamane: Preparation, crystal structure and high-temperature thermoelectric properties of double perovskite-type rare-earth cobalt ruthenium oxides. *J. Ceram. Soc. Jpn.* **115**, 792 (2007).

15. A.E. Smith, A.W. Sleight, and M. Subramanian: Electrical and magnetic properties of new rhodium perovskites: La_2MRhO_6, M = Cr, Fe, Cu. *Mater. Res. Bull.* **45**, 460 (2010).

16. T. Sugahara and M. Ohtaki: Structural and semiconductor-to-metal transitions of double-perovskite cobalt oxide $Sr_{2-x}La_xCoTiO_{6-\delta}$ with enhanced thermoelectric capability. *Appl. Phys. Lett.* **99**, 062107 (2011).

17. T. Sugahara, N. Van Nong, and M. Ohtaki: Structure and thermoelectric properties of $Ca_{2-x}Sr_x FeMoO_6$ ($0 \leq x \leq 0.3$) double-perovskite oxides. *Mater. Chem. Phys.* **133**, 630 (2012).

18. T. Sugahara, M. Ohtaki, and K. Suganuma: La doped effects on structure and thermoelectric properties of Sr_2MnMoO_6 double-perovskite oxides. *J. Asian Ceram. Soc.* **1**, 282 (2013).

19. P. Roy, V. Waghmare, and T. Maiti: Environmentally friendly $Ba_xSr_{2-x}TiFeO_6$ double perovskite with enhanced thermopower for high temperature thermoelectric power generation. *RSC Adv.* **6**, 54636 (2016).

20. P. Roy, V. Waghmare, K. Tanwar, and T. Maiti: Large change in thermopower with temperature driven p–n type conduction switching in environment friendly $Ba_xSr_{2-x}Ti_{0.8}Fe_{0.8}Nb_{0.4}O_6$ double perovskites. *Phys. Chem. Chem. Phys.* **19**, 5818 (2017).

21. P. Roy and T. Maiti: Colossal change in thermopower with temperature-driven p–n-type conduction switching in $La_xSr_{2-x}TiFeO_6$ double perovskites. *J. Phys. D: Appl. Phys.* **51**, 065104 (2018).

22. M. Saxena, P. Roy, M. Acharya, I. Bose, K. Tanwar, and T. Maiti: Enhanced thermoelectric figure-of-merit in environmentally benign $Ba_xSr_{2-x}TiCoO_6$ double perovskites. *Appl. Phys. Lett.* **109**, 263903 (2016).

23. M. Acharya and T. Maiti: Effect of bismuth doping on thermoelectric properties of Sr_2TiCoO_6. *Ferroelectrics* **532** (2018). (in press).

24. M. Saxena, K. Tanwar, and T. Maiti: Environmental friendly Sr_2TiMoO_6 double perovskite for high temperature thermoelectric applications. *Scr. Mater.* **130**, 205 (2017).

25. M. Saxena and T. Maiti: Metal-like electrical conductivity in $La_xSr_{2-x} TiMoO_6$ oxides for high temperature thermoelectric power generation. *Dalton Trans.* **46**, 5872 (2017).

26. M. Saxena and T. Maiti: Effect of Ba-doping on high temperature thermoelectric properties of Sr_2TiMoO_6 double perovskites. *J. Alloys Compd.* **710**, 472 (2017).

27. M. Saxena and T. Maiti: Evaluation of Ba doped $Sr_2TiFe_{0.5}Mo_{0.5}O_6$ double perovskites for high temperature thermoelectric power generation. *Scr. Mater.* **155**, 85 (2018).

28. M. Saxena and T. Maiti: Compositional modification of Sr_2TiCoO_6 double perovskites by Mo and La for high temperature thermoelectric applications. *Ceram. Int.* **44**, 2732 (2018).

29. K. Tanwar, M. Saxena, and T. Maiti: Enhancement of thermoelectric power factor of Sr_2CoMoO_6 double perovskite by annealing in reducing atmosphere. *J. Appl. Phys.* **122**, 164902 (2017).

30. P. Roy, V. Pal, and T. Maiti: Effect of spark plasma sintering (SPS) on the thermoelectric properties of $SrTiO_3$: 15 at.% Nb. *Ceram. Int.* **43**, 12809 (2017).

31. S. Ohta, T. Nomura, H. Ohta, and K. Koumoto: High-temperature carrier transport and thermoelectric properties of heavily La-or Nb-doped $SrTiO_3$ single crystals. *J. Appl. Phys.* **97**, 034106 (2005).

32. R. Funahashi, A. Kosuga, N. Miyasou, E. Takeuchi, S. Urata, K. Lee, H. Ohta, and K. Koumoto: Thermoelectric properties of $CaMnO_3$ system. In *Thermoelectrics, 2007. ICT 2007. 26th International Conference* (IEEE, Jeju Island, South Korea, 2007); p. 124.

33. L. Daniels, S. Ling, S. Savvin, M. Pitcher, M. Dyer, J. Claridge, B. Slater, F. Corà, J. Alaria, and M. Rosseinsky: A and B site doping of a phonon-glass perovskite oxide thermoelectric. *J. Mater. Chem. A* **6**, 15640–15652 (2018).

34. N. Nong, C-J. Liu, and M. Ohtaki: High-temperature thermoelectric properties of late rare earth-doped $Ca_3Co_4O_9 + \delta$. *J. Alloys Compd.* **509**, 977 (2011).

35. F. Zhang, Q. Lu, and J. Zhang: Synthesis and high temperature thermoelectric properties of $Ba_xAg_yCa_{3-x-y}Co_4O_9$ compounds. *J. Alloys Compd.* **484**, 550 (2009).

36. D. Sarma, E. Sampathkumaran, S. Ray, R. Nagarajan, S. Majumdar, A. Kumar, G. Nalini, and T.G. Row: Magnetoresistance in ordered and disordered double perovskite oxide, $Sr_2 FeMoO_6$. *Solid State Commun.* **114**, 465 (2000).

37. S. Kumar, G. Giovannetti, J. van den Brink, and S. Picozzi: Theoretical prediction of multiferroicity in double perovskite Y_2NiMnO_6. *Phys. Rev. B* **82**, 134429 (2010).

38. S. Vasala and M. Karppinen: $A_2B'B''O_6$ perovskites: A review. *Prog. Solid State Chem.* **43**, 1 (2015).

39. G. Demazeau, B. Siberchicot, S. Matar, C. Gayet, and A. Largeteau: A new ferromagnetic oxide La_2MnIrO_6: Synthesis, characterization, and calculation of its electronic structure. *J. Appl. Phys.* **75**, 4617 (1994).

40. O.N. Meetei, O. Erten, A. Mukherjee, M. Randeria, N. Trivedi, and P. Woodward: Theory of half-metallic double perovskites. I. Double exchange mechanism. *Phys. Rev. B* **87**, 165104 (2013).

41. P. Roy, I. Bose, and T. Maiti: Synthesis and characterization of Sr_2TiMO_6 (M = Fe, Co) double perovskites for high temperature thermoelectric applications. *Integr. Ferroelectr.* **174**, 34 (2016).

42. C.J. Howard, B.J. Kennedy, and P.M. Woodward: Ordered double perovskites—A group-theoretical analysis. *Acta Crystallogr., Sect. B: Struct. Sci.* **59**, 463 (2003).

43. M.T. Anderson, K.B. Greenwood, G.A. Taylor, and K.R. Poeppelmeier: B-cation arrangements in double perovskites. *Prog. Solid State Chem.* **22**, 197 (1993).

44. G. King and P.M. Woodward: Cation ordering in perovskites. *J. Mater. Chem.* **20**, 5785 (2010).

45. V. Goldschmidt: The laws of crystal chemistry. *Naturwissenschaften* **14**, 477 (1926).

46. J. Rodríguez-Carvajal: *An Introduction to the Program FullProf 2000* (Laboratoire Léon Brillouin, CEA-CNRS: Saclay, France, 2001).

47. B.K. Maji, H. Jena, R. Asuvathraman, and K.G. Kutty: Electrical conductivity and thermal expansion behavior of $MMoO_4$ (M = Ca, Sr, and Ba). *J. Alloys Compd.* **640**, 475 (2015).

48. D. Logvinovich, R. Aguiar, R. Robert, M. Trottmann, S. Ebbinghaus, A. Reller, and A. Weidenkaff: Synthesis, Mo-valence state, thermal stability and thermoelectric properties of $SrMoO_{3-x}N_x$ ($x > 1$) oxynitride perovskites. *J. Solid State Chem.* **180**, 2649 (2007).

49. G.A. Slack and M. Rowe: *CRC Handbook of Thermoelectrics* (CRC Press, Boca Raton, Florida, 1995); p. 407.

50. N. Wang, H. He, X. Li, L. Han, and C. Zhang: Enhanced thermoelectric properties of Nb-doped $SrTiO_3$ polycrystalline ceramic by titanate nanotube addition. *J. Alloys Compd.* **506**, 293 (2010).

51. T. Sugahara, M. Ohtaki, and T. Souma: Thermoelectric properties of double-perovskite oxide $Sr_{2-x}M_xFeMoO_6$ (M = Ba, La). *J. Ceram. Soc. Jpn.* **116**, 1278 (2008).

52. D. Ackerman, D. Moy, R. Potter, A. Anderson, and W. Lawless: Glassy behavior of crystalline solids at low temperatures. *Phys. Rev. B* **23**, 3886 (1981).

53. C. Huang: Some experimental aspects of spin glasses: A review. *J. Magn. Magn. Mater.* **51**, 1 (1985).

54. J. De Yoreo, R. Pohl, and G. Burns: Low-temperature thermal properties of ferroelectrics. *Phys. Rev. B* **32**, 5780 (1985).

55. K. Uchino and S. Nomura: Critical exponents of the dielectric constants in diffused-phase-transition crystals. *Ferroelectrics* **44**, 55 (1982).

56. G. Smolenskii and A. Agranovskaya: Dielectric polarization and losses of some complex compounds. *Zh. Tekh. Fiz.* **28**, 1380–1382 (1958).

57. D. Viehland, S. Jang, L.E. Cross, and M. Wuttig: Freezing of the polarization fluctuations in lead magnesium niobate relaxors. *J. Appl. Phys.* **68**, 2916 (1990).

58. D. Viehland, J. Li, S. Jang, L.E. Cross, and M. Wuttig: Dipolar-glass model for lead magnesium niobate. *Phys. Rev. B* **43**, 8316 (1991).

59. G. Burns and F. Dacol: Ferroelectrics with a glassy polarization phase. *Ferroelectrics* **104**, 25 (1990).

60. G. Burns and F. Dacol: Glassy polarization behavior in ferroelectric compounds Pb(Mg$_{13}$Nb$_{23}$)O$_3$ and Pb(Zn$_{13}$Nb$_{23}$)O$_3$. *Solid State Commun.* **48**, 853 (1983).

61. A. Bhalla, R. Guo, L. Cross, G. Burns, F. Dacol, and R.R. Neurgaonkar: Measurements of strain and the optical indices in the ferroelectric Ba$_{0.4}$Sr$_{0.6}$Nb$_2$O$_6$: Polarization effects. *Phys. Rev. B* **36**, 2030 (1987).

62. S. Shtrikman and E. Wohlfarth: The theory of the Vogel–Fulcher law of spin glasses. *Phys. Lett. A* **85**, 467 (1981).

63. R. Pirc and R. Blinc: Vogel–Fulcher freezing in relaxor ferroelectrics. *Phys. Rev. B* **76**, 020101 (2007).

64. T. Maiti, R. Guo, and A. Bhalla: Structure-property phase diagram of BaZr$_x$Ti$_{1-x}$O$_3$ system. *J. Am. Ceram. Soc.* **91**, 1769 (2008).

65. E. Fischer, W. Hässler, and E. Hegenbarth: Glass-like behaviour in the thermal conductivity of Sr$_{1-x}$Ba$_x$(Nb$_2$O$_6$) single crystal. *Phys. Status Solidi A* **72**, K169 (1982).

66. X. Yuan and M. Xu: Thermal transport properties of polycrystalline Pb$_2$FeMoO$_6$. *Mater. Res. Express* **5**, 066102 (2018).

67. H. Nakatsugawa, M. Saito, and Y. Okamoto: High-temperature thermoelectric properties of perovskite-type Pr$_{0.9}$Sr$_{0.1}$Mn$_{1-x}$Fe$_x$O$_3$ ($0 \leq x \leq 1$). *J. Electron. Mater.* **46**, 3262 (2017).

68. J-W. Moon, Y. Masuda, W-S. Seo, and K. Koumoto: Ca-doped HoCoO$_3$ as p-type oxide thermoelectric material. *Mater. Lett.* **48**, 225 (2001).

69. L. Daniels, S. Savvin, M. Pitcher, M. Dyer, J. Claridge, S. Ling, B. Slater, F. Corà, J. Alaria, and M. Rosseinsky: Phonon-glass electron-crystal behaviour by a site disorder in n-type thermoelectric oxides. *Energy Environ. Sci.* **10**, 1917 (2017).

70. R. Ang, Y. Sun, and W. Song: The magnetic, electrical and thermal transport studies in the layered cobalt oxide Nd$_{1-x}$Sr$_{1+x}$CoO$_4$ ($x = 0.25$ and 0.33). *J. Phys. D: Appl. Phys.* **40**, 5206 (2007).

71. Y. Wang, K.H. Lee, H. Ohta, and K. Koumoto: Thermoelectric properties of electron doped SrO(SrTiO$_3$)$_n$ ($n = 1, 2$) ceramics. *J. Appl. Phys.* **105**, 103701 (2009).

72. Y.F. Wang, K.H. Lee, H. Ohta, and K. Koumoto: Fabrication and thermoelectric properties of heavily rare-earth metal-doped SrO(SrTiO$_3$)$_n$ ($n = 1, 2$) ceramics. *Ceram. Int.* **34**, 849 (2008).

73. R. Sun, D. Li, L. Li, J. Zhang, Q. Wang, and X. Qin: Preparation and thermoelectric properties of rare-earth-metal-doped SrO(SrTiO$_3$)$_n$ oxides. *Procedia Eng.* **27**, 103 (2012).

74. K.H. Lee, S.W. Kim, H. Ohta, and K. Koumoto: Ruddlesden-popper phases as thermoelectric oxides: Nb-doped SrO(SrTiO$_3$)$_n$ ($n = 1, 2$). *J. Appl. Phys.* **100**, 063717 (2006).

75. P.W. Anderson: Absence of diffusion in certain random lattices. *Phys. Rev.* **109**, 1492 (1958).

76. P. Bernasconi, I. Biaggio, M. Zgonik, and P. Günter: Anisotropy of the electron and hole drift mobility in KNbO$_3$ and BaTiO$_3$. *Phys. Rev. Lett.* **78**, 106 (1997).

77. P.A. Cox: *Transition Metal Oxides: An Introduction to Their Electronic Structure and Properties* (Oxford University Press, New York, New York, 2010).

78. S. Lee, G. Yang, R.H. Wilke, S. Trolier-McKinstry, and C.A. Randall: Thermopower in highly reduced n-type ferroelectric and related perovskite oxides and the role of heterogeneous nonstoichiometry. *Phys. Rev. B* **79**, 134110 (2009).

79. K-Y. Yang, K-Z. Fung, and M-C. Wang: X-ray photoelectron spectroscopic and secondary ion mass spectroscopic examinations of metallic-lithium-activated donor doping process on La$_{0.56}$Li$_{0.33}$TiO$_3$ surface at room temperature. *J. Appl. Phys.* **100**, 056102-3 (2006).

80. I.C. Lekshmi, A. Gayen, and M. Hegde: The effect of strain on nonlinear temperature dependence of resistivity in SrMoO$_3$ and SrMoO$_{3-x}$N$_x$ films. *Mater. Res. Bull.* **40**, 93 (2005).

81. Y. Lu and C. Clayton: An XPS study of the passive and transpassive behavior of molybdenum in deaerated 0.1 M HCl. *Corros. Sci.* **29**, 927 (1989).

82. J-G. Choi and L. Thompson: XPS study of as-prepared and reduced molybdenum oxides. *Appl. Surf. Sci.* **93**, 143 (1996).

83. N.F. Mott and L. Friedman: Metal–insulator transitions in VO$_2$, Ti$_2$O$_3$, and Ti$_{2-x}$V$_x$O$_3$. *Philos. Mag.* **30**, 389 (1974).

84. E. Gorham-Bergeron and D. Emin: Phonon-assisted hopping due to interaction with both acoustical and optical phonons. *Phys. Rev. B* **15**, 3667 (1977).

85. N. Tsuda, K. Nasu, A. Fujimori, and K. Siratori: *Electronic Conduction in Oxides* (Springer Science & Business Media, New York, New York, 2013).

86. A. Nag and V. Shubha: Oxide thermoelectric materials: A structure–property relationship. *J. Electron. Mater.* **43**, 962 (2014).

87. P. Chaikin and G. Beni: Thermopower in the correlated hopping regime. *Phys. Rev. B* **13**, 647 (1976).

88. R. Waser and M. Aono: Nanoionics-based resistive switching memories. *Nat. Mater.* **6**, 833 (2007).

89. U. Chon, H.M. Jang, M. Kim, and C. Chang: Layered perovskites with giant spontaneous polarizations for nonvolatile memories. *Phys. Rev. Lett.* **89**, 087601 (2002).

90. S. Mathews, R. Ramesh, T. Venkatesan, and J. Benedetto: Ferroelectric field effect transistor based on epitaxial perovskite heterostructures. *Science* **276**, 238 (1997).

91. J.W. Fergus: Perovskite oxides for semiconductor-based gas sensors. *Sens. Actuators, B* **123**, 1169 (2007).

92. T. Yamashita and P. Hayes: Analysis of XPS spectra of Fe^{2+} and Fe^{3+} ions in oxide materials. *Appl. Surf. Sci.* **254**, 2441 (2008).

93. E. Paparazzo: XPS and auger spectroscopy studies on mixtures of the oxides SiO$_2$, Al$_2$O$_3$, Fe$_2$O$_3$, and Cr$_2$O$_3$. *J. Electron Spectrosc. Relat. Phenom.* **43**, 97 (1987).

94. H-R. Lee, S-J. Kim, I-S. Yang, and J-H. Choy: Low-dimensional and extended metal—metal bonded networks in transition metal compounds: Ba$_2$Nb$_5$O$_9$, Ba$_{2-x}$Y$_x$Nb$_5$O$_9$. *J. Solid State Chem.* **108**, 253 (1994).

95. C.J. Carmalt, T.D. Manning, I.P. Parkin, E.S. Peters, and A.L. Hector: Formation of a new (1T) trigonal NbS$_2$ polytype via atmospheric pressure chemical vapour deposition. *J. Mater. Chem.* **14**, 290 (2004).

96. A. Dementjev, O. Ivanova, L. Vasilyev, A. Naumkin, D. Nemirovsky, and D. Shalaev: Altered layer as sensitive initial chemical state indicator. *J. Vac. Sci. Technol., A* **12**, 423 (1994).

97. C. Lu, A. Kuang, and G. Huang: X-ray photoelectron spectroscopy study on composition and structure of sol–gel derived PbTiO$_3$ thin films. *J. Appl. Phys.* **80**, 202 (1996).

98. S.N. Guin, J. Pan, A. Bhowmik, D. Sanyal, U.V. Waghmare, and K. Biswas: Temperature dependent reversible p–n–p type conduction switching with colossal change in thermopower of semiconducting AgCuS. *J. Am. Chem. Soc.* **136**, 12712 (2014).

99. C. Xiao, X. Qin, J. Zhang, R. An, J. Xu, K. Li, B. Cao, J. Yang, B. Ye, and Y. Xie: High thermoelectric and reversible pnp conduction type switching integrated in dimetal chalcogenide. *J. Am. Chem. Soc.* **134**, 18460 (2012).

100. T. Nilges, S. Lange, M. Bawohl, J.M. Deckwart, M. Janssen, H-D. Wiemhöfer, R. Decourt, B. Chevalier, J. Vannahme, and H. Eckert: Reversible switching between p-and n-type conduction in the semiconductor Ag$_{10}$Te$_4$Br$_3$. *Nat. Mater.* **8**, 101 (2009).

101. R. Littleton, IV, T.M. Tritt, J. Kolis, D. Ketchum, N.D. Lowhorn, and M. Korzenski: Suppression of the resistivity anomaly and corresponding thermopower behavior in the pentatelluride system by the addition of Sb: Hf$_{1-X}$Zr$_X$Te$_{5-Y}$Sb$_Y$. *Phys. Rev. B* **64**, 121104 (2001).

102. O. Osters, M. Bawohl, J-L. Bobet, B. Chevalier, R. Decourt, and T. Nilges: A conceptional approach to materials for resistivity switching and thermoelectrics. *Solid State Sci.* **13**, 944 (2011).